



This discussion paper is/has been under review for the journal Hydrology and Earth System Sciences (HESS). Please refer to the corresponding final paper in HESS if available.

Energy fluxes and surface characteristics over a cultivated area in Benin: daily and seasonal dynamics

O. Mamadou^{1,2}, J. M. Cohard³, S. Galle¹, C. N. Awanou², A. Diedhiou¹,
B. Kounouhewa², and C. Peugeot⁴

¹IRD, LTHE, UMR5564, CNRS/UJF-Grenoble 1/G-INP/IRD, 38041 Grenoble, France

²Laboratoire de Physique du Rayonnement, Faculté des Sciences et Techniques, Université d'Abomey-Calavi, Abomey-Calavi, Benin

³UJF-Grenoble 1, LTHE, UMR5564, CNRS/UJF-Grenoble 1/G-INP/IRD, 38041 Grenoble, France

⁴IRD, HSM, UMR5569, CNRS/UM1/UM2, 34095 Montpellier, France

Received: 9 July 2013 – Accepted: 30 July 2013 – Published: 16 August 2013

Correspondence to: O. Mamadou (ossenatou.mamadou@ujf-grenoble.fr)

Published by Copernicus Publications on behalf of the European Geosciences Union.

Title Page

Abstract

Introduction

Conclusions

References

Tables

Figures

◀

▶

◀

▶

Back

Close

Full Screen / Esc

Printer-friendly Version

Interactive Discussion



Abstract

Latent and sensible heat fluxes are known as key factors in the West African monsoon dynamics. However, few long-term observations of these land surface fluxes are available to document their impact in the climate variability of this region. The present study took advantage of the Sudanian site of the AMMA-CATCH (African Monsoon Multidisciplinary Analysis – Coupling the Tropical Atmosphere and Hydrological Cycle) observatory where turbulent fluxes were measured using the eddy covariance technique. One full year of data of energy budget over a cultivated site located in northern Benin was examined. Four contrasted seasons were identified and detailed focusing on their corresponding daily cycles. The flux partitioning was investigated through the evaporative fraction (EF) and the Bowen ratio (β) at both seasonal and daily scales. Finally, the surface conductance (G_s) and the decoupling coefficient (Ω) were calculated and confronted with specific bare soil or canopy models to identify the main processes for each season.

The results pointed out the contrasted seasonal variations of sensible and latent heat fluxes due to changing atmospheric and surface conditions. During the wet season, surface conditions barely affected EF, which remained in steady regime (EF = 0.75), while latent heat flux was dominant and β was about 0.4. During the transitional periods, both EF and β were highly variable. A low but significant evapotranspiration was measured in the dry season (EF = 0.08) attributed to few scattered bushes, distributed on a bare area, possibly fed by the water table. Nevertheless, sensible heat fluxes were largely dominant ($\beta \sim 10$) during dry season. Moreover, β revealed the ligneous vegetation flowering dynamics during the dry season. The results also showed a strong surface atmosphere coupling, which suggests a systematic mixing of the flow within the canopy with the atmospheric surface layer whatever the atmospheric conditions and vegetation height. Modeling approaches showed the good agreement of soil evaporation with the Sakaguchi bare soil model. Transpiration was also well reproduced with the Collatz stomata model. Finally, skin surface temperature had large seasonal and

HESSD

10, 10605–10657, 2013

Daily and seasonal dynamics

O. Mamadou et al.

Title Page

Abstract

Introduction

Conclusions

References

Tables

Figures

◀

▶

◀

▶

Back

Close

Full Screen / Esc

Printer-friendly Version

Interactive Discussion



daily amplitude and played a major role for all surface processes. As a consequence, the modeling of surface temperature is crucial to represent correctly energy and water budget for this region.

1 Introduction

5 Since the pioneering work of Charney (1975), the effects of soil moisture on climate, and thus surface–atmosphere exchanges have been underlined (Eltahir, 1998), and shown to be of major importance in West Africa (Parker et al., 2005). These theoretical and simulated (Koster et al., 2004) interactions have been observed in the Sahel. Taylor and Lebel (1998) have shown that the frequency of rain was increased
10 over moist Sahelian soils, and Taylor et al. (2012) have shown that convection triggering was enhanced over the interfaces between wet and dry areas. The influence of surface–atmosphere exchanges on precipitation is not limited to event scale but has also been observed at seasonal scale. Philippon and Fontaine (2002) suggested that the Guinean rainy season affects the following Sahelian rainy season several weeks
15 later. The residual soil moisture at the end of the rainy season was found to delay vegetation transpiration and thus increase atmospheric humidity. Indeed during the dry season, deep-rooted trees can take advantage of the water table. Although vegetation activity has been shown to influence the monsoon dynamics through modeling studies (Xue and Shukla, 1993; Zheng et al., 1999), very few observations support these
20 results. This was also emphasize by the ALMIP experiment, which was designed to assess the ability of land surface models to simulate correctly the West African water and energy balance at regional scale (Boone et al., 2009a). In this context, the first aim of this paper is to document the seasonal variation of latent (LE) and sensible heat (H) fluxes in Sudanian region where surface–atmosphere exchanges are expected to
25 affect monsoon dynamics.

Few experimental surface–atmosphere exchanges data sets have been analyzed for long periods including the different phases of the monsoon. The Sahelian climate fluxes

Daily and seasonal dynamics

O. Mamadou et al.

Title Page

Abstract

Introduction

Conclusions

References

Tables

Figures

◀

▶

◀

▶

Back

Close

Full Screen / Esc

Printer-friendly Version

Interactive Discussion



Daily and seasonal dynamics

O. Mamadou et al.

[Title Page](#)[Abstract](#)[Introduction](#)[Conclusions](#)[References](#)[Tables](#)[Figures](#)[⏪](#)[⏩](#)[◀](#)[▶](#)[Back](#)[Close](#)[Full Screen / Esc](#)[Printer-friendly Version](#)[Interactive Discussion](#)

have been documented for periods of a few weeks (Kabat et al., 1997; Schüttemeyer et al., 2006) and annual periods (Bagayoko et al., 2007; Brümmer et al., 2008), but to the authors' knowledge, Sudanian climate has been studied only for few weeks in the dry to wet transition period in Nigeria (Mauder et al., 2007). Thus only partial conclusions in the seasonal and daily variability of surface fluxes were drawn for the Sudanian region.

The AMMA-CATCH (African Monsoon Multidisciplinary Analysis – Coupling the Tropical Atmosphere and Hydrological Cycle) observing system (Lebel et al., 2009) was designed to provide an unprecedented set of surface flux data covering several vegetation types over contrasted sites ranging from 9.5° N to 17° N in latitude. The flux data sets have been presented in Ramier et al. (2009) and Timouk et al. (2009) for the Sahelian locations. The southern AMMA-CATCH site is located in northern Benin (Fig. 1) under Sudanian climate (~ 1200 mm of rainfall per year). It was equipped at several places with rainfall, soil moisture, meteorological, latent and sensible heat flux measurements allowing for water and energy budget monitoring. Previous studies carried out on this region have highlighted the marked seasonal dynamics of surface exchanges due to changing atmospheric and land surface conditions. Lothon et al. (2008) and Lohou et al. (2010) focused on the impact of entrainment on observed turbulent characteristics at the surface but did not relate those flux measurements to surface characteristics. Guyot et al. (2012) used infrared scintillometry observations over a 2.4 km path length capping heterogeneous vegetation including crops and savannah. They found that the partition of the daily available energy reached a constant regime during the wet season. Moreover, during the dry season, the estimated evapotranspiration rates were found to be correlated with water table discharge (Guyot et al., 2009; Descloitres et al., 2011) for an area with heterogeneous land cover.

One of the northern Benin site eddy covariance (EC) systems was installed over a cultivated area that consists of small crop fields intricate with shrub areas and some isolated trees. This land use covers 25 % of northern Benin and is in continuous expansion. Indeed, in West Africa, the population growth rate (2.57 %) is one of the most

Daily and seasonal dynamics

O. Mamadou et al.

[Title Page](#)[Abstract](#)[Introduction](#)[Conclusions](#)[References](#)[Tables](#)[Figures](#)[|◀](#)[▶|](#)[◀](#)[▶](#)[Back](#)[Close](#)[Full Screen / Esc](#)[Printer-friendly Version](#)[Interactive Discussion](#)

significant in the world (UN, 2011). The population has increased by a factor of four from 1950 to 2010 in this region, and is expected to double by 2050 according to the UN population most optimistic projection (UN, 2011). This resulted in a significant conversion of areas with natural vegetation into cultivated areas (CSAO, 2012; Judex et al., 2009) and may have induced a modification of the dynamics of water and energy exchanges between the continental surface and the atmosphere.

In this paper, a full year of eddy covariance surface fluxes measured over a cultivated site is presented. The energy fluxes are quantified and analyzed at the seasonal and daily timescales, and a major focus is presented on four contrasted periods. These four 15-day periods are chosen to build robust daily composite of energy fluxes to quantify daily characteristics. Data quality control is presented, including energy balance closure and footprint analysis. Finally, surface processes are identified assessing and comparing surface conductance from field data and from classical models for bare soil conductance (Sellers et al., 1992; Lee and Pielke, 1992; Sakaguchi and Zeng, 2009) and stomata conductance (Collatz et al., 1992).

The site, the data processing and useful diagnostics are described in Sect. 2. In Sect. 3, seasonal and daily cycles of energy fluxes are analyzed. Processes are discussed in Sect. 4 with surface variables such as the evaporative fraction, the Bowen ratio and the surface conductance.

2 Material and methods

2.1 Study area

The so-called “Nalohou” site is located in northern Benin in the Donga Department (Fig. 1). In this region, the rainfall regime is driven by the seasonal migration of the Intertropical Convergence Zone (ITCZ) with 90 % of the annual rainfall falling in seven months (April to October), and a mean rainfall amount of 1190 mm (1950–2002) (Lelay et al., 2005).

**Daily and seasonal
dynamics**

O. Mamadou et al.

[Title Page](#)[Abstract](#)[Introduction](#)[Conclusions](#)[References](#)[Tables](#)[Figures](#)[◀](#)[▶](#)[◀](#)[▶](#)[Back](#)[Close](#)[Full Screen / Esc](#)[Printer-friendly Version](#)[Interactive Discussion](#)

The landscape is rather flat with local slope of about 3% overlying metamorphic crystalline bedrock. The main soils are “ferric lixisols” (Faure and Volkoff, 1998). The surface textural properties correspond to a loamy sand surface with high permeability, whereas the underlying weathered bedrock contains deep clayey layers with high retention properties (De Condappa et al., 2008).

The flux tower was installed near the Nalohou village (lat 9.74° N, long 1.60° E; 449 m a.s.l), in a cultivated area. It is located in an herbaceous fallow, surrounded by small fields (< 1 ha) with a large variety of rain-fed annual crops (cassava, yam, maize, and groundnut) (Fig. 4). Crop rotation, in an agroforestry context, is the main farming practice in the area. Fallow areas are commonly covered by scattered shrubs, overlaid by a dense herbaceous layer during the wet season. The herbaceous layer usually starts growing in April after the first rains and reaches its maximum in October (height up to 2.5 m). Bushfire is a traditional farmer practice in Benin; the vegetation (mainly the herbaceous layer) is burnt between November and February, when the soil and vegetation are dry. Hence, during the dry season, the soil is bare for about 5 months. Isolated trees (with height < 10 m) are frequently encountered in the fields, and fallows are present in the neighborhood of the flux tower. These land cover distributions are typical of the northern Benin region.

The water table at the tower site is close to the surface and varies, on average, between 1.5 m in September and 5 m in June (Séguis et al., 2011). The Ara stream, bordered by a riparian forest, flows 250 m north from the tower, and a wet area commonly called *bas-fond* is located 70 m westward. The latter can contribute to the fluxes measured at tower site for westerly winds. Although it is not the main wind direction, this situation has to be considered to interpret some flux measurements.

2.2 Instrumentation and data processing

The meteorological variables (wind speed and direction, air temperature and humidity, the four components of surface radiative budget) were measured at 2 m height; the rainfall was measured with a tipping bucket rain gauge. The ground measurements

Daily and seasonal dynamics

O. Mamadou et al.

Title Page

Abstract

Introduction

Conclusions

References

Tables

Figures

◀

▶

◀

▶

Back

Close

Full Screen / Esc

Printer-friendly Version

Interactive Discussion



included soil temperature (−10, −20 and −40 cm) and average soil moisture between 5 and 30 cm. All the measurements were recorded at a 30 min time step. All the sensor characteristics are reported in Table 1. The vegetation height was monitored at a 20-day time step, and the leaf area index (LAI) time series is a combination of satellite LAI products (CYCLOPE, MODIS, SEVIRI), constrained by in situ measurements derived from hemispherical photographs based on the method proposed by Weiss et al. (2004).

The eddy covariance system used in this study consisted in a fast-response three-dimensional sonic anemometer (CSAT3, Campbell Sci., Logan (UT), USA) and a fast response open-path infrared gas analyzer (LI-7500, LI-COR, Lincoln (NE), USA). They were installed at 4.95 m above the ground and measured 3-D wind speed, temperature, water vapor and CO₂ concentration at a 20 Hz sampling rate.

Half-hourly average of sensible (H) and latent heat (LE) fluxes were calculated according to theoretical Eqs. (1) and (2) using CarboEurope protocol (Aubinet et al., 1999), where ρ is the air density (kg m^{-3}), C_p the heat capacity at constant pressure ($\text{J kg}^{-1} \text{K}^{-1}$), λ the latent heat of vaporization (J g^{-1}), T' the air temperature fluctuation (K), q' the absolute humidity fluctuation (g m^{-3}) and w' the vertical wind speed fluctuation (m s^{-1}).

$$H = \rho C_p \overline{w' T'}; \quad (1)$$

$$\text{LE} = \lambda \overline{w' q'}. \quad (2)$$

The data were processed with the EdiRe software (version 1.5.0.28 at University of Edinburgh). The procedure included despiking and double rotation of 3-D wind speed to nullify the vertical wind velocity (Kaimal and Finnigan, 1994; Aubinet et al., 1999). Sonic air temperature was corrected for changes in humidity and pressure (Schotanus et al., 1983) and for variations in air density due to water vapor (Webb et al., 1980). Time lag corrections were applied to account for time delay of air samples between the sonic anemometer and the gas analyzer. Finally, corrections for frequency response were made in order to account for flux underestimation due to instrument separation and scale filtering of each sensor (Moore, 1986).

[Title Page](#)[Abstract](#)[Introduction](#)[Conclusions](#)[References](#)[Tables](#)[Figures](#)[◀](#)[▶](#)[◀](#)[▶](#)[Back](#)[Close](#)[Full Screen / Esc](#)[Printer-friendly Version](#)[Interactive Discussion](#)

In addition to this data processing, the data corresponding to rainy events and the following 30 min were not considered because the hygrometer is known to be very sensitive to raindrop extinction (Culf et al., 1997). Finally, the data were filtered using the non-stationarity criteria suggested by Mauder and Foken (2004). These tests filtered out situations when the flux magnitude or the wind direction varied too much within the 30 min averaging period. During the selected periods (defined below), these tests eliminated 4 % of H and 5 % of LE in P1, 20 % of H and 37 % of LE in P2, 35 % of H and 55 % of LE in P3, 25 % of H and 30 % of LE in P4.

2.3 Surface diagnostics

2.3.1 Energy balance

Energy balance closure is an independent and efficient diagnosis to check the consistency of scalar fluxes measured by an eddy covariance system (Aubinet et al., 1999). According to the surface energy budget, Eq. (3) compares the available energy ($R_n - G$) with the sum of turbulent fluxes at a half-hourly time step.

$$R_n - G = H + LE \quad (3)$$

R_n is the net radiation (Wm^{-2}), and G the ground heat flux (Wm^{-2}). The net radiation was calculated from measured incoming and outgoing short- and longwave radiations. The soil heat flux was estimated from soil temperature and moisture profiles using the harmonic method (Guyot et al., 2009), based on the estimation of the heat diffusion coefficient from the soil temperature at two depths. Thermal conductivity was computed using soil moisture measurements and the volumetric heat capacity of soil and water.

2.3.2 Derivation of surface parameters

The surface conductance G_s (ms^{-1}) quantifies the ability of the soil or the canopy to transfer water to the atmosphere. It was calculated from flux measurements using

inverted Penman–Monteith relationship (Eq. 4), where G_a (m s^{-1}) is the aerodynamic conductance and was computed according to Eq. (5); Δ (Pa K^{-1}) is the slope of the saturation curve, γ (Pa K^{-1}) the psychrometric constant, VPD (Pa) the vapor pressure deficit, and $\beta = H/LE$ the Bowen ratio defined as the ratio of the sensible to the latent heat flux.

$$G_s = \left[\frac{1}{G_a} \left(\frac{\Delta}{\gamma} \beta - 1 \right) + \frac{\rho C_p \text{VPD}}{\gamma (R_n - G)} (\beta + 1) \right]^{-1} \quad (4)$$

$$G_a = \frac{u_*^2 \phi_H}{u \phi_m} \quad (5)$$

In Eq. (5), u_* is the friction velocity, and ϕ_m and ϕ_H are the Businger–Dyer stability functions (Businger et al., 1971). Following Jarvis and McNaughton (1986), the decoupling coefficient Ω was calculated with Eq. (6). This coefficient varies between 0 when vapor deficit in the vicinity of the surface equals vapor deficit in the atmosphere (coupling conditions) and 1 when vapor deficit near the surface is imposed by the surface itself (de-coupling conditions).

$$\Omega = \frac{\Delta/\gamma + 1}{\Delta/\gamma + 1 + G_a/G_s} \quad (6)$$

Finally, the evaporative fraction EF, which represents the fraction of the available energy that is converted into evapotranspiration, was calculated with (Eq. 7).

$$\text{EF} = \frac{LE}{H + LE} \quad (7)$$

All these diagnostic variables were computed at a half-hourly time step and were used to build composite diurnal cycles. Midday averages (10:00–14:00) were also computed to analyze the annual cycle. Times are given in UTC.

Title Page

Abstract

Introduction

Conclusions

References

Tables

Figures

◀

▶

◀

▶

Back

Close

Full Screen / Esc

Printer-friendly Version

Interactive Discussion



3 Results

3.1 A contrasted seasonal cycle

Figures 2 and 3 illustrate the 2008 annual cycle of the atmospheric variables, the surface conditions and the components of the radiative budget at the surface. From these figures, the Sudanian climate may be characterized by a succession of wet and dry seasons separated by two dry-to-wet and wet-to-dry transition periods. These four seasons, driven by the monsoon cycle, are characterized by highly contrasted atmospheric and surface conditions, which lead to contrasted sensible and latent fluxes dynamics. Different authors (Sultan and Janicot, 2003; Lothon et al., 2008) have found that the zonal wind and the water vapor mixing ratio (WVMR) can be used to define seasons. In this study, the absolute humidity (q_a) was preferred to WVMR for seasons delimitation because it was a direct measurement from the gas analyzer and did not change drastically the season definition proposed in the previous studies. The dry season ($q_a < 6 \text{ gm}^{-3}$) and the wet season ($q_a > 16 \text{ gm}^{-3}$) are represented respectively by “rose and blue” shaded areas in Figs. 2, 3, 6 and 10. The four seasons are described below together with four 15-day periods that were chosen to characterize the atmospheric conditions and the surface response characteristics prevailing during each stage of the monsoon cycle. The four studied periods have been chosen for their quasi-steady-state thermodynamic conditions, and the quasi-absence of rain (except during the wet season), which ensured a good availability and quality of the eddy covariance data. These periods have the same number of days, which makes their statistical characteristics as comparable as possible. The following sections exhibit the characteristics of each season and focus on these periods.

3.1.1 Dry season and period 1 “P1”: from 18 January to 1 February 2008

The dry season was characterized by a steady low q_a and dry north-easterly Harmattan wind that consists in a light to moderate breeze (mean 2.4 ms^{-1}), bringing dry air ($q_a <$

HESSD

10, 10605–10657, 2013

Daily and seasonal dynamics

O. Mamadou et al.

Title Page

Abstract

Introduction

Conclusions

References

Tables

Figures

◀

▶

◀

▶

Back

Close

Full Screen / Esc

Printer-friendly Version

Interactive Discussion



5 5 g m^{-3} ; VPD $\sim 2.3 \text{ kPa}$). The surface conditions were dry and the soils remained bare as no rain occurred. The water content in the 30 cm top layer was $\sim 12 \text{ mm}$ (Fig. 2g).

During the first 15-day period (P1), typical for the dry season, the daily mean air temperature was 23°C (Fig. 2e, Table 2). The net shortwave radiation (SWnet, Fig. 3a) was substantially low (maxima at $\sim 666 \text{ W m}^{-2}$) due firstly to the presence of aerosols brought by Harmattan that reduced the incoming shortwave radiation, and secondly due to the surface albedo, which was relatively high (~ 0.19 , Fig. 3c) because of dry bare soil conditions. The longwave radiative budget (LWnet) was negative all year long (Table 2), corresponding to an energy loss. During the P1 period, these strong energy losses reflected both high surface temperature and low atmosphere water content (Fig. 3b). Their minimum, maximum and mean values were respectively -235 W m^{-2} , -65 W m^{-2} and -118 W m^{-2} . Both short- and longwave radiative budgets resulted in low net radiation values as it will be observed in Fig. 6. Under Sudanian climate, these steady dry conditions usually last less than two months around January (Fig. 2).

15 **3.1.2 Dry to wet season and period 2 “P2”: from 26 February to 11 March 2008**

The “moistening transition season” (from dry to wet season) is characterized by monsoon flux intrusions. These can be observed in the wind direction time series (Fig. 2c), which abruptly alternates from north to south during the daily cycle. It is one of the atmospheric signatures of the moistening season: humid south-westerly winds were observed at night, bringing moist air up to 18 g m^{-3} in the lowest levels of the atmosphere. These wet layers were mixed in the whole boundary layer during the following day when the convection developed and dry north-easterly conditions prevailed (Lothon et al., 2008). These peculiar dynamical conditions were due to the large scale daily ITCZ oscillations and the vertical development of the boundary layer (Pospichal et al., 2010; Lohou et al., 2010). This lead to a gradual increase of absolute humidity with irregular day-to-day variability (Fig. 2b). During this period, isolated but important rainfalls were observed and the vegetation began to develop.

Title Page

Abstract

Introduction

Conclusions

References

Tables

Figures

◀

▶

◀

▶

Back

Close

Full Screen / Esc

Printer-friendly Version

Interactive Discussion



The second 15-day period (P2) has been defined as typical of the moistening season. The q_a variability is captured during P2 since its daily mean oscillates between 5 and 15 gm^{-3} . Surface and radiation conditions were not so different from those of the P1 period. The surface was still bare and dry; albedo values were about 0.2 (Fig. 3c) and the net shortwave was similar to that observed in P1 with a slightly higher maximum. Even though increasing as compared to P1, LWnet was still strongly negative meaning the surface was still warm at this period of the year (Fig. 3b).

3.1.3 Wet season and period 3 “P3”: from 7 July to 21 July 2008

The wet season was characterized by the moist southerly monsoon flow. The wind direction was well established at 240° . Rainfall frequency increased after the wet season onset because of a higher occurrence of mesoscale convective events. During this season, the absolute humidity was remarkably stable ($\sim 18 \text{ gm}^{-3}$) with a low day-to-day variability (Fig. 2b). The wet season ended when northerly wind conditions came back.

The P3 period was chosen after the monsoon onset that occurred on 22 June 2008 according to the definition proposed by Sultan and Janicot (2003). Nine rainy days were observed during this 15-day period, cumulating 97 mm of rainfall. The high soil water storage ($\sim 35 \text{ mm}$, Fig. 2g) favored the development of the herbaceous layer ($\text{LAI} \sim 1.5 \text{ m}^2 \text{ m}^{-2}$, Fig. 2g). The net shortwave radiation shows strong day-to-day variability (Fig. 3a). These variations were related to changes in cloud cover, which reduced substantially the incoming shortwave radiation. Because of the vegetation cover and the wet state of the surface, the albedo reached lower values than in the dry season (~ 0.15 , Fig. 3c) and the outgoing shortwave radiation was reduced. In turn, the surface cooling reduced outgoing longwave radiation and thus increased the net longwave radiation, which reached its highest mean daily value (-37 W m^{-2}) (Fig. 3b, Table 2). During period P3, the daily air temperature range was less than 10°C with daily mean of about 24°C . These wet conditions corresponded to a small atmospheric demand as the VPD daily mean was 0.6 kPa (Fig. 2f).

Title Page

Abstract

Introduction

Conclusions

References

Tables

Figures

◀

▶

◀

▶

Back

Close

Full Screen / Esc

Printer-friendly Version

Interactive Discussion



3.1.4 Wet to dry season and period 4 “P4”: from 24 October to 7 November 2008

At the end of the rainy season, when almost no rain occurred, the crops were harvested and the remaining senescent annual vegetation was burnt mid-November. The surface soil began to dry but was not completely dried out (Fig. 2g). The wind direction changed ($\sim 70^\circ$), but south-westerly conditions were observed time to time, which brought moisture and sometimes rainfall.

The period P4 was chosen 7 days after the last rainy event of the wet season. The mean air temperature was close to that of the wet season (25°C , Table 2), but the daily range was much higher (17°C). At this time, the vegetation height was the highest, but the senescence phase had begun, as shown in the LAI trend (Fig. 2g). Thus, the albedo reached its lowest yearly value (~ 0.13 , Fig. 3c). The net shortwave radiation increased (mean daily maximum of 760Wm^{-2}) for three reasons: albedo decrease, clear sky conditions (Fig. 3a) and low nebulosity. The net longwave radiation increased slightly (daily mean of -67Wm^{-2}) as the surface dried and surface temperature increased.

3.2 Spatial representativity of the eddy covariance measurements

As it was introduced before, Sudanian landscapes are a mix of various little fields and natural land cover. In such a context, a footprint analysis is necessary to ensure data representativity. It is presented for each period. Among numerous footprint approaches developed in the past decades (Horst and Weil, 1992; Hsieh et al., 1997; Hsieh et al., 2000; Schmid, 2002; Kljun et al., 2004), the simple analytical Hsieh 1-D model (Hsieh et al., 2000) with a 2-D extension (Detto et al., 2006) was chosen because of its explicit formulation for a 2-D diffusive footprint calculation. The footprint model was applied to the half-hourly flux data to get a succession of 2-D distribution functions of the sensible heat flux contributions. During daytime, the good convective situations generated small footprint, whereas at night, when the atmosphere is slightly stratified, the footprint had larger extension (not shown). Average footprints weighted by the corresponding sensible heat fluxes were processed to take into account the strength of the source of each

HESSD

10, 10605–10657, 2013

Daily and seasonal dynamics

O. Mamadou et al.

Title Page

Abstract

Introduction

Conclusions

References

Tables

Figures

◀

▶

◀

▶

Back

Close

Full Screen / Esc

Printer-friendly Version

Interactive Discussion



30 min contribution. Figure 4 presents the average footprint for each selected period superimposed over a Google Earth image (April 2010). Each iso-contour corresponds to a contribution of 25 %, 50 % and 75 %, respectively, to the observed sensible heat flux. During period P1 (Fig. 4a), the measurements were likely affected by some shrubs in the upwind direction. The riparian forest located to the north of the site (which appears at the top of the image) was far enough not to contribute to the measurements. During period P2 (Fig. 4b), wind direction varied a lot, but the footprint mainly remained over bare soil areas. Although daytime winds were mainly north-easterly winds, south-westerly night winds also significantly contribute to the footprint as this forcing lasted after sunrise. Thus, the *bas-fond* area, which is surrounded by trees, was partly included in the footprint. During this period, southerly winds were also observed from time to time. For these conditions, some isolated trees were likely to contribute to the measured fluxes. During period P3 (Fig. 4c), the wind direction has moved to the south-west. A 0.6 m high herbaceous layer has grown almost everywhere around the flux station in such a way that most of the shrubs were overlaid by grass, and the turbulent flows were only disturbed by some isolated trees. Finally during period P4 (Fig. 4d), vegetation was high (~ 2.5 m) and thus increased the roughness length (0.4 m) and the displacement height (1.6 m). For these vegetated conditions, footprint areas were reduced by a factor of two and the contributing areas were much closer to the sensor.

The contributions of fallows or annual crops to 75 % of the footprint area were respectively 87 %, 87 %, 77 % and 97 % from periods P1 to P4. During period P3, the measurements were slightly more affected by the surrounding trees. To conclude, the flux measurements presented below were considered as well representative of the so-called cultivated area for the four studied periods.

3.3 Energy balance closure

The energy balance closure was computed for the whole year and for the four 15-day periods (Table 3). Scatterplot of $LE + H$ vs. $R_n - G$ are shown in Fig. 5. At a 30 min timescale, the determination coefficient r^2 ranges from 0.90 to 0.97, which indicated

Title Page

Abstract

Introduction

Conclusions

References

Tables

Figures

◀

▶

◀

▶

Back

Close

Full Screen / Esc

Printer-friendly Version

Interactive Discussion



Daily and seasonal dynamics

O. Mamadou et al.

[Title Page](#)[Abstract](#)[Introduction](#)[Conclusions](#)[References](#)[Tables](#)[Figures](#)[|◀](#)[▶|](#)[◀](#)[▶](#)[Back](#)[Close](#)[Full Screen / Esc](#)[Printer-friendly Version](#)[Interactive Discussion](#)

that more than 90 % of the variability in the observed turbulent fluxes can be explained by the available energy. Considering the whole year (Fig. 5a), the linear regression coefficient (0.84) indicates a 16 % of non-closure, which corresponds to an underestimation of $H + LE$ as compared to $Rn - G$. However, the energy balance closure varies, depending on the period of the year. During period P1, the determination coefficient was the highest (97 %), but the slope of the regression line was higher than one (1.1). This is due to midday values for which the $H + LE$ is larger than $Rn - G$. This suggests an underestimation of the available energy, which can be explained by dust deposits on the sensor. The sensor opacity impacts net radiation, mostly when the sun is high in the sky. For values lower than 250 W m^{-2} , available energy and turbulent fluxes were well correlated. However, the turbulent fluxes could be affected by errors, but biases were not detectable. Statistical confidence was quantified from the standard deviation of the residuals. The uncertainty on turbulent fluxes and particularly in the sensible heat flux for this period was estimated to $\pm 8 \%$. This percentage corresponds to the ratio of the standard deviation of the residuals divided by the maximum value of H .

During period P2, the slope was 1.04 implying a good balance closure (Fig. 5c). The larger scatter for high ($Rn - G$) values was partly due to Rn measurements that were again partly affected by dust since the sensor had not been cleaned up since the middle of the period. The statistical confidence on turbulent fluxes for this period was $\pm 16 \%$.

For the last two periods P3 and P4 (Fig. 5d and e), the regression coefficient was significantly lower than one, indicating a strong (-25% to -20%) underestimation of turbulent fluxes. Because of systematic power shortages during the night, which stopped the gas analyzer until 09:00 in period P3, the low values of turbulent fluxes ($< 200 \text{ W m}^{-2}$) were only due to evening fluxes. For period P4, the pattern of the scatterplot looks similar to that of period P3. Indeed, evening turbulent fluxes were larger than the available energy. However, morning values were available for period P4 and produced a typical out-of-phase pattern (“8”-shaped) for the energy budget scatterplot (Fig. 4d). This may be due to the vegetation cover, which played as a buffer and induced

Daily and seasonal dynamics

O. Mamadou et al.

Title Page

Abstract

Introduction

Conclusions

References

Tables

Figures

◀

▶

◀

▶

Back

Close

Full Screen / Esc

Printer-friendly Version

Interactive Discussion



a time shift in the daily peak of the soil heat flux. As a result, some hysteresis or asymmetry appeared. However, this canopy storage effect is known to account for one or two tens of Wm^{-2} , which does not explain the hundreds (Wm^{-2}) of non-closure errors observed. This only can explain a part of the energy imbalance observed in P4 and P3.

5 Considering that the net radiation was unbiased during these periods, the three other energy budget terms cumulate the imbalance proportionally to their absolute values.

Although imperfect, the energy balance closure presented in this study is similar or better than what is commonly found with eddy covariance method in previous studies (Wilson et al., 2002) and especially in the West African regions (Mauder et al., 2007; 10 Bagayoko et al., 2007; Brümmner et al., 2008; Ramier et al., 2009; Timouk et al., 2009). In the light of the following daily cycle analysis, it can reasonably be concluded that consistency and quality of the various flux components are satisfactory.

3.4 Seasonal and daily dynamics of energy budget terms

The annual cycle of the four energy budget components is shown in Fig. 6. The shaded 15 areas show the large daily amplitude for all budget terms. One can notice the low values of the net radiation in dry season ($< 500 \text{Wm}^{-2}$). The sensible heat flux H over bare soil had a rather steady behavior, alike net radiation. The daily average and the peak reached respectively 80Wm^{-2} and 330Wm^{-2} . During the wet season, R_n was as high as 800Wm^{-2} but with a large day-to-day variability due to the cloud cover; the 20 average sensible heat flux was rapidly divided by a factor of two. Then, H increased slowly at the end of the wet season when vegetation dried and rainfall stopped. The latent heat fluxes (LE) had an opposite behavior with very low values during dry and transition seasons and high evapotranspiration rates during the wet season (daily maximum values up to 450Wm^{-2}). The soil heat flux was almost zero at a daily time step 25 but showed wide daily amplitude. When rainfall occurred on hot soil surface (DOY 95, Fig. 3b), sharp drops in ground heat fluxes were observed; these negative values correspond to a rapid release of energy that fed evaporation processes.

Daily and seasonal dynamics

O. Mamadou et al.

[Title Page](#)[Abstract](#)[Introduction](#)[Conclusions](#)[References](#)[Tables](#)[Figures](#)[◀](#)[▶](#)[◀](#)[▶](#)[Back](#)[Close](#)[Full Screen / Esc](#)[Printer-friendly Version](#)[Interactive Discussion](#)

In the light of the energy fluxes time series, every chosen period was well representative of the corresponding season. This is illustrated with Fig. 7 where box plots of midday (10:00–14:00) sensible heat fluxes are presented for each period and each season. The median value of period P1 was slightly higher than for the whole dry season (+20 W m⁻²), but the difference was less than 7% of midday value. The sensible heat flux variability during P2 was largely reduced as compared with the whole moistening season because a period without any rainy event was chosen. Nevertheless, the median value of P2 was close to the seasonal median value. For the period P3, sensible heat fluxes were at their lowest daily values as it can be observed in Fig. 6b. Finally, drying season was hard to catch with a single 15-day period because climatic and surface conditions changed a lot during this transition season. To summarize, P1 and P2 (resp. P3) represented the highest (resp. lowest) sensible heat flux regime, while P4 was only representative of the beginning of the wet-to-dry transition season with decaying herbaceous vegetation.

The following paragraphs focus on the four 15-day periods, and more precisely on the daily cycles of Rn, H, LE and G. In order to draw robust conclusions, daily composites of each energy budget term have been computed. They are reported in Fig. 8a–d. Table 2 regroups daily statistical characteristics including daily means, min and max daily values and their respective standard deviation for each period.

For period P1 (Fig. 8a), Rn shows a “bell-shaped” pattern, typical of clear sky conditions. However, it reached its lowest daily maximum ($442 \pm 29 \text{ W m}^{-2}$) and minimum ($-96 \pm 7 \text{ W m}^{-2}$) due to high aerosol concentration brought by the Harmattan wind, the strong surface albedo (~ 0.2) and a large surface temperature amplitude ($18^\circ\text{--}50^\circ\text{C}$) (not shown). The maximum value was reached just before noon because of a large LWnet amplitude that increased till 13:30 and reached -170 W m^{-2} (Fig. 3b). During this period, G was in phase with the daily course of net radiation. It ranged between $-88 \pm 6 \text{ W m}^{-2}$ at night and $174 \pm 11 \text{ W m}^{-2}$ just before noon (Table 2). Despite the high surface temperature and hence the high temperature gradient in the soil, G was limited by the low thermal conductivity of the dry soil ($0.56 \text{ W m}^{-1} \text{ K}^{-1}$). During nighttime hours,

Daily and seasonal dynamics

O. Mamadou et al.

[Title Page](#)[Abstract](#)[Introduction](#)[Conclusions](#)[References](#)[Tables](#)[Figures](#)[◀](#)[▶](#)[◀](#)[▶](#)[Back](#)[Close](#)[Full Screen / Esc](#)[Printer-friendly Version](#)[Interactive Discussion](#)

G did not compensate R_n entirely, and negative sensible heat fluxes were observed ($-26 \pm 10 \text{ W m}^{-2}$). During daytime, the sensible heat flux H was also bell-shaped, but slightly shifted after noon. As the surface was hot and dry, the available energy was mainly converted into H , which reached its maximum of $326 \pm 40 \text{ W m}^{-2}$ at 12:30. It remained positive one hour later than R_n since the atmospheric stability systematically became positive at 18:00 during this period (Fig. 9a). By contrast, LE was low but non-zero, although the soil was bare and the surface was dry. Its daily maximum value was $17 \pm 4 \text{ W m}^{-2}$. This non-negligible amount of evapotranspiration may have originated from the transpiration of shrubs and sparse trees, located northward as shown in the footprint analysis (Fig. 4a). The soil evaporation was also able to contribute as the 0–30 cm soil water storage was still slightly decreasing during this period (Fig. 2g).

The P2 period is rather similar to period P1 since the soil was still bare. During this period no rainfall occurred, while air and surface temperature increased, which increased the time shift between the sensible heat flux and the net radiation. At night, the absolute sensible heat flux was lower because of weaker wind and weaker absolute temperature gradient (Fig. 13d). Changes in wind direction and moisture supply from night monsoon flow did not affect surface processes much, but added some scattering in the day-to-day variability since the footprint explored all the directions around the sensor (Fig. 4b). This is particularly obvious on latent heat flux statistics (Table 2). However, the slight increase of LE could be attributed to an enhancement of shrub activity. Indeed, Seghieri et al. (2009) have shown that in Sudanian climate shrub flowering is probably linked to the rise of air temperature, occurring from February to May in the study region. Bearing in mind that the flowering involves a significant activity of plants, this means that shrubs should have a higher transpiration activity in P2 and could also explain the increase in latent heat flux between P1 and P2. Thus, the latent heat flux was low (Fig. 8b) but not null in dry season under Sudanian climate even if the soil surface remains dry.

During period P3 (Fig. 8c), the occurrence of rainfalls changed drastically both atmospheric and surface conditions; the annual vegetation has grown. Surface temperature

(not shown) had low daily amplitude (25° – 32° C) as the soil was moist due to regular rainfalls. As a consequence, the net radiation was lower (not so negative) all night long ($-37 \pm 13 \text{ W m}^{-2}$) till 06:00 in the morning. Afternoon hours were less cloudy than in the morning, and the maximum daily Rn was observed at 13:00. The daily cycle of Rn directly affected turbulent fluxes, which showed the same midday shape. The surface conditions were favorable to LE, which was the main consumer of the available energy. LE peaked at $259 \pm 58 \text{ W m}^{-2}$. However, sensible and ground heat fluxes were found to be non-negligible with respective maximum daily values of $103 \pm 38 \text{ W m}^{-2}$ and $88 \pm 35 \text{ W m}^{-2}$. It was also quite surprising to observe positive latent heat fluxes in the evening till midnight (Fig. 8c) (no LE observation was available later). As $(\overline{w'q'})$ covariance was always positive, this was not attributed to flux corrections. During the night, the stability was slightly positive (0.1 ± 0.1), which characterized a near-neutral surface layer (Fig. 9c). This process may be fed by the release of energy stored into the ground since available energy is positive until midnight (i.e., $R_n > G$ in Fig. 8c). Mauder et al. (2007) also observed positive latent heat fluxes at night in Nigeria, which were attributed to the advection of dry air over a wet surface. However, in our case it was not attributable to dry air advection as no changes in wind direction were observed during P3.

During P4, clear sky conditions had come back, but the net radiation was decreasing rapidly as the daily course of the sun was not so high and the surface temperature increased, which lowered longwave net radiation (Fig. 6a). The daily cycle of Rn reached its maximum at noon ($625 \pm 78 \text{ W m}^{-2}$) as well as other energy budget terms. During this period, soil and vegetation were drying, and the daily maximum of latent heat flux decreased (Fig. 8d). At night, LE fell to zero, one hour after Rn turned negative. This is different from the previous period P3 because night stability (Fig. 9d) was near unity in P4 while it was near neutral during period P3. G daily dynamic showed a two-hour delay in the morning as compared to the Rn dynamic. This explained the out-of-phase pattern already observed on energy budget closure (Fig. 5d). This was supposed to be caused by the 2.5 m high vegetation layer, which induced a delay in

Daily and seasonal dynamics

O. Mamadou et al.

Title Page

Abstract

Introduction

Conclusions

References

Tables

Figures

◀

▶

◀

▶

Back

Close

Full Screen / Esc

Printer-friendly Version

Interactive Discussion



soil surface warming, whereas turbulent fluxes and net radiation followed the dynamics of the canopy top skin temperature (Santanello and Friedl, 2003). Finally, one has to remember that the surface conditions changed during this season and little generality can be derived from this P4 period analysis.

The following section discusses and analyzes energy partitioning with classical synthetic variables such as evaporative fraction, Bowen ratio and surface conductance, to identify more general characteristics of this Sudanian cultivated area and to derive useful parameters for soil–vegetation–atmosphere transfer (SVAT) modeling like specific PFT (plant functional type).

4 Characterization of surface processes and discussion

4.1 Energy partitioning and surface characteristics

The midday average evaporative fraction (10:00–14:00) (EF) is presented in Fig. 10a to examine the seasonal variations in energy partitioning related to surface conditions. Two contrasted surface behaviors were identified: during the dry season, from January to the end of February, very low evaporation occurred ($EF = 0.08$); during this period, the soil was bare and dry (Fig. 2g). On the contrary, when surface soil water storage exceeded 30 mm, EF remained high ($EF = 0.75$) with limited variations. During four months the soil water content variations and the vegetation development did not affect EF. This second period matched with the second part of the wet season, after the monsoon onset (22 June 2008; DOY 173). Between these two periods, EF was highly variable depending on soil water availability, vegetation development, and vegetation stress. These fluctuations were due to isolated rainfall events, which usually occur during the transition periods. The dynamics of EF associated with such an isolated rainfall is clearly illustrated in Fig. 10a: the heavy rainfall that occurred on DOY 324 (20 November 2008) over bare soil, after vegetation burning, resulted in an instantaneous increase of EF from 0.2 to 0.75 followed by a 10-day decrease. A more

Title Page

Abstract

Introduction

Conclusions

References

Tables

Figures

◀

▶

◀

▶

Back

Close

Full Screen / Esc

Printer-friendly Version

Interactive Discussion



detailed analysis of surface response and recovery associated with rainfall events is presented in Lohou et al. (2013) for all AMMA-CATCH flux sites.

The Bowen ratio plotted on the same graph (Fig. 10a) shows an opposite behavior. One can notice the decrease of β starting around DOY 30, which is interpreted as the signature of the ligneous vegetation dynamics (transpiration), in a period where neither rain nor change in soil moisture was observed. Indeed, the maximal value of β was phased with trees or shrub leaf renewal (Seghieri et al., 2009), with increasing LE synchronous with leaf development.

The observed conductance G_s and de-coupling factor Ω are plotted in Fig. 10b for the whole year. During the dry season, when the soil was bare, G_s was less than 1 mm s^{-1} and the de-coupling factor was almost null. This means that surface and atmosphere were coupled, because the surface layer close to the ground was very unstable and thus the mixing imposed the atmospheric water vapor deficit near the ground. After the monsoon onset, when vegetation had grown enough and soil moisture was no longer limiting vegetation activity (after DOY 174), the canopy conductance reached 20 mm s^{-1} with a maximum value around 30 mm s^{-1} . This corresponds to usual crop conductance values as observed by Bagayoko et al. (2007) in Burkina Faso. The de-coupling factor was still far from unity and remained below 0.7. This means that complete de-coupling between atmosphere and canopy water vapor deficit was never observed even when the vegetation was fully developed: the atmosphere was unstable enough to mix the air inside the canopy with the boundary layer. At the end of the wet season, the decrease of soil moisture and LAI resulted in a concomitant decrease of both the conductance and the de-coupling parameter.

To analyze the sensitivity of energy partitioning to the surface conditions along the annual cycle, EF vs. G_s at midday is plotted in Fig. 11. The graph shows that EF was highly influenced by the surface conductance when G_s values are lower than 10 mm s^{-1} , as observed in the P1, P2 and P4 periods. On the contrary, EF was not driven by the surface conditions any longer when G_s was higher than this threshold value. It was the case in the P3 period and more generally after the onset (DOY 174),

HESSD

10, 10605–10657, 2013

Daily and seasonal dynamics

O. Mamadou et al.

Title Page

Abstract

Introduction

Conclusions

References

Tables

Figures

◀

▶

◀

▶

Back

Close

Full Screen / Esc

Printer-friendly Version

Interactive Discussion



and evaporation was only driven by the atmosphere demand and the available solar radiation.

4.2 Daily cycles of surface and aerodynamic conductances

Hereafter, the surface conductance G_s is discussed to understand better the relative control of surface conditions during the daily cycle. The observations were compared to modeling results of specific processes like bare soil evaporation and canopy transpiration. The aim of this comparison is to identify predominant processes and to check the ability of standard model to reproduce these observations in Sudanian climate conditions.

Surface conductance is the sum of the canopy and the bare soil conductances, which have specific formulations and may account for different water vapor deficit. For bare soils, the surface water vapor conductance is mainly limited by the soil resistance (r_{soil}), which depends on soil moisture, whereas the canopy conductance is regulated by more complex photosynthetic processes, soil moisture availability, etc. Advantage was taken of the contrasted surface conditions found in Benin to explore the soil resistance (r_{soil}) behavior when the soil was bare at the beginning of the year. The canopy conductance was assessed when vegetation had grown, and can be modeled by a “big leaf” approach (Jarvis and McNaughton, 1986). For the Nalohou site, these conditions were achieved in the second part of the rainy season. During this period, light extinction in the vegetation cover prevented significant soil evaporation.

The soil resistance ($r_{\text{soil}} = 1/G_s$) is considered when soil is entirely bare (DOY 1–124 and 313–366) and plotted against surface soil moisture measured at 5 cm depth (Fig. 12). The soil resistance increased rapidly when soil moisture reached the residual saturation ($0.02 \text{ m}^3 \text{ m}^{-3}$). For higher surface soil moisture, between $0.02 \text{ m}^3 \text{ m}^{-3}$ and $0.15 \text{ m}^3 \text{ m}^{-3}$, it decreased following a power law as observed by previous authors (van de Griend and Owe, 1994; Aluwihare and Watanabe, 2003). The r_{soil} modeling laws proposed by Sellers et al. (1992), Lee and Pielke (1992), and Sakaguchi and Zeng (2009) have been plotted in Fig. 12 to verify the ability of these bare soil models to

Daily and seasonal dynamics

O. Mamadou et al.

Title Page

Abstract

Introduction

Conclusions

References

Tables

Figures

◀

▶

◀

▶

Back

Close

Full Screen / Esc

Printer-friendly Version

Interactive Discussion



Daily and seasonal dynamics

O. Mamadou et al.

Title Page

Abstract

Introduction

Conclusions

References

Tables

Figures

◀

▶

◀

▶

Back

Close

Full Screen / Esc

Printer-friendly Version

Interactive Discussion



capture the behavior of bare soil conductance in tropical conditions. It can be seen that Seller's formulation overestimates r_{soil} for all soil moisture values. Thus, this model will systematically underestimate bare soil evaporation. Similarly, the Lee and Pielke r_{soil} function underestimates evaporation, but for low soil moisture values only. The Sakaguchi and Zeng function fit much better with the data. However, none of these models were able to reproduce the high values of the bare soil conductance observed for dry conditions, when the soil matric potential was high, but this would not affect too much bare soil evaporation since very little water is available at the surface for these conditions.

In order to analyze more precisely the flux partitioning and the surface control on evapotranspiration, the average daily cycles of aerodynamic and soil/canopy conductance are plotted for the four periods in Fig. 13. For periods P1 and P2, the soil was bare and the surface conductance was very low all day long ($< 01 \text{ mm s}^{-1}$) as already discussed. For these two periods, the aerodynamic conductances were quite similar except between 02:00 and 06:00 (Fig. 13c). During the wet period (P3), G_a had the same daily magnitude as during preceding periods and reached 90 mm s^{-1} . However, G_a remained as high as 30 mm s^{-1} during the night. This means that the atmospheric resistance to vapor transfer is low at night during this period, and thus turbulent surface–atmosphere exchanges, enhanced by wind shear, are possible as it was observed for LE (Fig. 8c). During period P3, the daily cycle of G_s was affected by gaps in the data sets during the night. However, the valid fraction of the data sets shows that when the vegetation was fully developed, the daily cycle of G_s was clearly dissymmetric, with higher values in the morning. For period P4 (wet-to-dry transition), the aerodynamic conductance at midday was much higher than in the other periods, due to a higher roughness length when herbaceous vegetation was high. In this period, G_a was also the lowest during the night because of higher stability (Fig. 9d). The surface conductance G_s of the senescent vegetation was high (24 mm s^{-1}) in the morning (07:00) and similar to the one observed in P3, but it decreased rapidly. It was four times lower than in P3 at 09:00; the midday G_s value was much lower (3 mm s^{-1}) than during period P3.

Daily and seasonal dynamics

O. Mamadou et al.

[Title Page](#)[Abstract](#)[Introduction](#)[Conclusions](#)[References](#)[Tables](#)[Figures](#)[|◀](#)[▶|](#)[◀](#)[▶](#)[Back](#)[Close](#)[Full Screen / Esc](#)[Printer-friendly Version](#)[Interactive Discussion](#)

Transpiration processes have been modeled in order to interpret conductance G_s dynamics during the wet season and in particular during periods P3 and P4. We used the Ball–Berry stomata conductance model as described by Collatz et al. (1992) for C4 vegetation. The conductance model was extracted from CLM4 land surface model (see chapter 8 of CLM4 technical note, Thornton, 2010).

A C4 grass was chosen for stomata characteristics (PFT). The required atmospheric (air temperature, precipitation, humidity) and surface (LAI, soil moisture) forcing conditions are those presented in Fig. 2. The photosynthetically active radiation (PAR) was calculated as a fraction (0.5) of the observed incoming shortwave radiation for both sun-lighted and shaded leaves. Leaf temperature was assessed from outgoing long-wave radiation measurements using Stefan–Boltzmann law and a 0.97 emissivity for leaves. In the following, only vegetated surface conditions were considered (from DOY 189 to DOY 313), including P3. Three typical days in the wet season have been chosen to illustrate observed and simulated G_s dynamics in relation with rainfall (Fig. 14). During these 3 days, large G_s peaks were observed not only after the rainy events (12 and 14 September), but also in the morning whereas no rain had been observed the day before (13 September). As these peaks were not simulated by the Ball–Berry stomata conductance model, we hypothesized that the observed G_s peaks were caused by evaporation of either intercepted water or dew deposits; these processes are not parameterized in the stomata model. As eddy covariance data were not available in the morning during period P3, the systematic dew deposition cannot be assessed during this period. However, low vapor pressure deficit (< 200 Pa) was observed at night between air and leaf surface (Fig. 2f).

Symmetric (12 September) and dissymmetric daily patterns were observed with higher values in the morning (13 September): when vegetation temperature overpassed 30°C , a temperature limitation of photosynthesis can be observed, as stated by Collatz et al. (1992). In addition to evaporation from intercepted water, the vegetation temperature often overpassed 30°C in the early afternoon during P3 and P4 (not

shown). This explains why, in P3 and P4 periods, the Gs values were higher in the morning than in the afternoon (Fig. 13a).

To quantify the model ability to simulate the conductance beyond these 3 days, the observed vs. simulated Gs values were plotted for the whole vegetated period (Fig. 15).

To remove dew or rainfall effect, the three hours after sunrise and the six hours after rainfall have been excluded from the analysis. Figure 15 shows that the conductance was satisfactorily simulated ($r^2 = 0.92$) by the Ball–Berry model, with the default C4 grass parameter set. Then we can interpret that corresponding moisture flux EC data were observations of a predominant transpiration process during daytime. The temperature effect was also well reproduced and had to be taken into account in SVAT modeling. Any SVAT simulation producing a leaf temperature bias will also produce a bias on evapotranspiration rate. In particular in this Sudanian region, leaf temperature during daytime varies around the most efficient temperature ($\sim 30^\circ\text{C}$). Then photosynthesis regime is often close to its maximum, and any negative or positive bias in leaf temperature will lead to an underestimation of canopy conductance and then of transpiration.

4.3 Daily cycle of evaporative fraction (EF)

The composite daily cycle of EF from 06:00 to 18:00 (Fig. 16) shows a typical “concave up” shape with a minimum around 12:00. In the morning, before 09:00, EF is noisy because negative sensible or latent heat fluxes can lead to low values of the sum ($H + LE$), which leads to large values in EF. In period P3, the continuous increase of EF during daytime from 09:00 (0.69) to 16:00 (0.80) and the higher surface conductance in the morning (Fig. 13a) seem contradictory. Gentine et al. (2007) extensively studied EF and simulated an increase of EF in late afternoon due to thermal inversion into the canopy when vegetation temperature was greater than soil temperature. Such inversions, characterized by $EF > 1$, were not really observed in Nalohou except very late in the afternoon (18:00) during P3. This EF daily increase was better explained by Gentine et al. (2012), who also showed that this trend can be due to time shift between

Title Page

Abstract

Introduction

Conclusions

References

Tables

Figures

◀

▶

◀

▶

Back

Close

Full Screen / Esc

Printer-friendly Version

Interactive Discussion



HESSD

10, 10605–10657, 2013

Daily and seasonal dynamics

O. Mamadou et al.

[Title Page](#)[Abstract](#)[Introduction](#)[Conclusions](#)[References](#)[Tables](#)[Figures](#)[◀](#)[▶](#)[◀](#)[▶](#)[Back](#)[Close](#)[Full Screen / Esc](#)[Printer-friendly Version](#)[Interactive Discussion](#)

sensible and latent heat fluxes. This delay was observed for period P3 when the maximum value of the latent heat flux was observed later than the sensible heat flux one. Such behavior resulted from a slower surface temperature increase in the morning time compared to the net radiation dynamics. This was caused by the large evapotranspiration rate during period P3, which attenuated the sensible heat flux daily temporal dynamics. During period P4, EF daily cycle exhibits a pronounced but typical U shape, resulting from the rapid decrease in sensible heat flux before 18:00 (Fig. 8d) because of the rapid radiative cooling (Figs. 3b and 13d) and subsequent stratification (Fig. 9d). During periods P1 and P2, EF was very low and showed negligible differences along the day. Although clear in Fig. 8a and b, the time shift of sensible heat fluxes observed has no marked effect on the daily increase of EF (Fig. 16).

5 Conclusions

Although the West African region is considered as a hot spot for climatic and water resources studies, few long-term climatic observations are available. This is particularly the case for surface–atmosphere flux data sets. In this study, a full year of energy budget data was presented and analyzed, corresponding to a typical patchy cultivated area composed of a mix of crop and fallows, in northern Benin. This location is considered representative of the Sudanian climate, characterized by alternating contrasted seasons. The interpretation of the data set was supported by an extensive footprint analysis. Four periods representative of the dry, the wet, and the dry-to-wet and wet-to-dry transition seasons have been defined and used throughout the analysis. The data set has been analyzed for each period within a systematic framework including seasonal and daily cycle timescales. The evaporative fraction, the Bowen ratio and the surface conductance have been computed from the observations and compared to the theoretical predictions of specific models in order to evaluate and improve our understanding of the underlying processes. The main outcomes of this work can be summarized in the following paragraphs.

HESSD

10, 10605–10657, 2013

Daily and seasonal dynamics

O. Mamadou et al.

[Title Page](#)[Abstract](#)[Introduction](#)[Conclusions](#)[References](#)[Tables](#)[Figures](#)[◀](#)[▶](#)[◀](#)[▶](#)[Back](#)[Close](#)[Full Screen / Esc](#)[Printer-friendly Version](#)[Interactive Discussion](#)

A complete seasonal cycle has been characterized including daily average and amplitude for all energy budget terms. The constant EF regime was confirmed during the wet season ($EF = 0.75$). Some non-zero evapotranspiration rates were detected in the dry season ($EF \sim 0.08$). These low LE values were attributed to the transpiration of the bushes and trees embedded in the eddy covariance footprint. Data quality was precise enough to detect some surface and vegetation processes like the signature of leaf renewal, which seems to be captured in the Bowen ratio dynamics (maximum value in the dry season). The Sakaguchi and Zeng (2009) soil resistance model well fit the soil evaporation data selected during the dry season.

Each season has been characterized by a representative composite diurnal cycle analyzed with regard to its atmospheric and surface characteristics. During the wet season, after the onset, soil moisture no longer limits transpiration ($G_s > 10 \text{ mm s}^{-1}$). The EF slightly increases during the day, and evapotranspiration was observed until midnight. This favorable period for rain-fed crops lasts almost four months. The atmospheric water vapor deficit was always imposed at leaf surfaces (low values of the de-coupling coefficient). The Ball–Berry stomata conductance model (Collatz et al., 1992) was found to be adapted to simulate accurately the transpiration processes for this cultivated area using a C4 PFT parameter set. EF daily cycles exhibited a typical U shape except during wet season when evaporation and transpiration processes slow down the surface temperature increase and then shift in the afternoon heat flux maxima.

Finally, the skin surface temperature had a large seasonal and daily amplitude and played a major role for all surface processes by (i) increasing the longwave radiation (thus limiting the net radiation during the dry season); (ii) increasing ground heat fluxes and energy storage (thus limiting transpiration during the wet season); and controlling C4 vegetation transpiration. As a consequence, surface temperature has to be accurately simulated and then evaluated to ensure a correct simulation of all energy fluxes under Sudanian climate. The observation described in this paper should be useful for SVAT model evaluation and in particular for the ALMIP-II experiment (Boone et al.,

2009b), for which meso- and local-scale modeling results will be compared with in situ measurements.

Acknowledgements. The AMMA-CATCH observing system (<http://www.amma-catch.org/>) has been funded since 2001 by IRD, INSU and the French Ministry of Research, in cooperation with the Direction Générale de l'Eau (DG-Eau), Benin. The Nalohou flux station was supported by the Ouémé-2025 project (French FSP-RIPIECSA program). The article processing charges have been funded by INSU-CNRS. The authors wish to thank particularly the researchers and technicians who helped them during the different steps of this work: G. Quantin, R. Biron, M. Le Gall and the Beninese technicians T. Ouani, S. Afouda, M. Wubda, S. Alloganvinon and J. Sogba-Goh for their permanent support in the field. This work was made possible by the financial support provided by the IRD-DSF, AUF-Bureau de l'Afrique de l'Ouest and Université d'Abomey-Calavi (Benin).



The publication of this article is financed by CNRS-INSU.

References

- Aluwihare, S. and Watanabe, K.: Measurement of evaporation on bare soil and estimating surface resistance, *J. Environ. Eng.*, 129, 1157–1168, 2003.
- Aubinet, M., Grelle, A., Ibrom, A., Rannik, Ü, Moncrieff, J., Foken, T., Kowalski, A. S., Martin, P. H., Berbigier, P., Bernhofer, C., Clement, R., Elbers, J., Granier, A., Grünwald, T., Morgenstern, K., Pilegaard, K., Rebmann, C., Snijders, W., Valentini, R., and Vesala, T.: Estimates of the annual net carbon and water exchange of forests: the EUROFLUX methodology, *Adv. Ecol. Res.*, 30, 113–175, 1999.
- Bagayoko, F., Yonkeu, S., Elbers, J., and van de Giesen, N.: Energy partitioning over the West African savanna: multi-year evaporation and surface conductance measurements in eastern Burkina Faso, *J. Hydrol.*, 334, 545–559, 2007.

Daily and seasonal dynamics

O. Mamadou et al.

Title Page

Abstract

Introduction

Conclusions

References

Tables

Figures

◀

▶

◀

▶

Back

Close

Full Screen / Esc

Printer-friendly Version

Interactive Discussion



Daily and seasonal dynamics

O. Mamadou et al.

Title Page

Abstract

Introduction

Conclusions

References

Tables

Figures

◀

▶

◀

▶

Back

Close

Full Screen / Esc

Printer-friendly Version

Interactive Discussion



- Boone, A., Decharme, B., Guichard, F., de Rosnay, P., Balsamo, G., Beljaars, A., Chopin, F., Orgeval, T., Polcher, J., Delire, C., Ducharne, A., Gascoïn, S., Grippa, M., Jarlan, L., Ker-goat, L., Mougin, E., Gusev, Y., Nasonova, O., Harris, P., Taylor, C., Norgaard, A., Sandholt, I., Otlé, C., Pocard–Leclercq, I., Saux–Picart, S., and Xue, Y.: The AMMA Land Surface Model Intercomparison Project (ALMIP), *B. Am. Meteorol. Soc.*, 90, 1865–1880, 2009a.
- Boone, A., Getirana, A. C. V., Demarty, J., Cappelaere, B., Galle, S., Grippa, M., Lebel, T., Mougin, E., Peugeot, C., and Vischel, T.: The African Monsoon Multidisciplinary Analyses (AMMA) Land Surface Model Intercomparison Project Phase 2 (ALMIP2), *GEWEX News*, 19, 9–10, 2009b.
- Brümmer, C., Falk, U., Papen, H., Szarzynski, J., Wassmann, R., and Brüggemann, N.: Diurnal, seasonal, and interannual variation in carbon dioxide and energy exchange in shrub savanna in Burkina Faso (West Africa), *J. Geophys. Res.*, 113, G02030, doi:10.1029/2007JG000583, 2008.
- Businger, J. A., Wyngaard, J. C., Izumi, Y., and Bradley, E. F.: Flux–profile relationships in the atmospheric surface layer, *J. Atmos. Sci.*, 28, 181–189, 1971.
- Charney, J. G.: Dynamics of deserts and drought in the Sahel, *Q. J. Roy. Meteorol. Soc.*, 101, 193–202, 1975.
- Collatz, G. J., Ribas–Carbo, M., and Berry, J. A.: Coupled photosynthesis–stomatal conduc-tance model for leaves of C4 plants, *Funct. Plant Biol.*, 19, 519–538, 1992.
- CSAO: Compte rendu du forum du club du sahel et de l’Afrique de l’Ouest, Peuplement, marché et sécurité alimentaire, Ouagadougou, 4–8 December 2012, 16 pp., available at: <http://www.oecd.org/fr/csao/publications/FR-Compte%20rendu%20forum.pdf> (last access: 19 June 2013), 2012.
- Culf, A. D., Foken, T., and Gash, J. H. C.: The energy balance closure problem, in: *Vegetation, water, humans and the climate. A new perspective on an interactive system*, edited by: Kabat, P., Claussen, M., Whitlock, S., Gash, J. H. C., Bravo de Guenni, L., Meybeck, M., Pielke, R., Vörösmarty, C. J., Hutjes, R. W. A., and Lütke-meier, S., Springer, Berlin, Heidelberg, 159–166, 2004.
- De Condappa, D., Galle, S., Dewandel, B., and Haverkamp, R.: Bimodal zone of the soil textural triangle: common in tropical and subtropical regions, *Soil Sci. Soc. Am. J.*, 72, 33–40, 2008.
- Descloitres, M., Séguis, L., Legchenko, A., Wubda, M., Guyot, A., and Cohard, J. M.: The contribution of MRS and resistivity methods to the interpretation of actual evapo–transpiration

Daily and seasonal dynamics

O. Mamadou et al.

Title Page

Abstract

Introduction

Conclusions

References

Tables

Figures

◀

▶

◀

▶

Back

Close

Full Screen / Esc

Printer-friendly Version

Interactive Discussion



measurements: a case study in metamorphic context in north Benin, *Near Surf. Geophys.*, 9, 187–200, 2011.

Detto, M., Montaldo, N., Albertson, J. D., Mancini, M., and Katul, G.: Soil moisture and vegetation controls on evapotranspiration in a heterogeneous Mediterranean ecosystem on Sardinia, Italy, *Water Resour. Res.*, 42, W08419, doi:10.1029/2005WR004693, 2006.

Eltahir, E. A.: A soil moisture–rainfall feedback mechanism, 1. Theory and observations, *Water Resour. Res.*, 34, 765–776, 1998.

Faure, P. and Volkoff, B.: Some factors affecting regional differentiation of the soils in the Republic of Benin (West Africa), *Catena*, 32, 281–306, 1998.

Gentine, P., Entekhabi, D., Chehbouni, A., Boulet, G., and Duchemin, B.: Analysis of evaporative fraction diurnal behaviour, *Agr. Forest Meteorol.*, 143, 13–29, 2007.

Gentine, P., Entekhabi, D., and Polcher, J.: The diurnal behavior of evaporative fraction in the soil–vegetation–atmospheric boundary layer continuum, *J. Hydrometeorol.*, 12, 1530–1546, 2012.

Guyot, A., Cohard, J.-M., Anquetin, S., Galle, S., and Lloyd, C. R.: Combined analysis of energy and water balances to estimate latent heat flux of a sudanian small catchment, *J. Hydrol.*, 375, 227–240, 2009.

Guyot, A., Cohard, J.-M., Anquetin, S., and Galle, S.: Long-term observations of turbulent fluxes over heterogeneous vegetation using scintillometry and additional observations: a contribution to AMMA under Sudano–Sahelian climate, *Agr. Forest Meteorol.*, 154–155, 84–98, 2012.

Horst, T. W. and Weil, J. C.: Footprint estimation for scalar flux measurements in the atmospheric surface layer, *Bound.-Lay. Meteorol.*, 59, 279–296, 1992.

Hsieh, C.-I., Katul, G. G., Schieldge, J., Sigmon, J. T., and Knoerr, K. K.: The Lagrangian Stochastic Model for fetch and latent heat flux estimation above uniform and nonuniform terrain, *Water Resour. Res.*, 33, 427–438, 1997.

Hsieh, C.-I., Katul, G., and Chi, T.: An approximate analytical model for footprint estimation of scalar fluxes in thermally stratified atmospheric flows, *Adv. Water Resour.*, 23, 765–772, 2000.

Jarvis, P. G. and McNaughton, K. G.: Stomatal control of transpiration: scaling up from leaf to region, *Adv. Ecol. Res.*, 15, 49 pp., 1986.

Judex, M., Thamm, H.-P., Röhrig, J., and Schulz, O.: IMPETUS Atlas du Bénin Résultats de recherche 2000–2007, Département de Géographie, University of Bonn, Germany, 2009.

Daily and seasonal dynamics

O. Mamadou et al.

[Title Page](#)[Abstract](#)[Introduction](#)[Conclusions](#)[References](#)[Tables](#)[Figures](#)[◀](#)[▶](#)[◀](#)[▶](#)[Back](#)[Close](#)[Full Screen / Esc](#)[Printer-friendly Version](#)[Interactive Discussion](#)

- Kabat, P., Dolman, A. J., and Elbers, J. A.: Evaporation, sensible heat and canopy conductance of fallow savannah and patterned woodland in the Sahel, *J. Hydrol.*, 188, 494–515, 1997.
- Kaimal, J. C. and Finnigan, J. J.: *Atmospheric Boundary Layer Flows: Their Structure and Measurement*, Oxford University Press, 1994.
- 5 Kljun, N., Calanca, P., Rotach, M. W., and Schmid, H. P.: A simple parameterisation for flux footprint predictions, *Bound.-Lay. Meteorol.*, 112, 503–523, 2004.
- Koster, R. D., Dirmeyer, P. A., Guo, Z., Bonan, G., Chan, E., Cox, P., Gordon, C. T., Kanae, S., Kowalczyk, E., Lawrence, D., Liu, P., Lu, C.–H., Malyshev, S., McAvaney, B., Mitchell, K., Mocko, D., Oki, T., Oleson, K., Pitman, A., Sud, Y. C., Taylor, C. M., Verseghy, D., Vasic, R.,
10 Xue, Y., and Yamada, T. (The GLACE Team): Regions of strong coupling between soil moisture and precipitation, *Science*, 305, 1138–1140, 2004.
- Lebel, T., Parker, D. J., Flamant, C., Bourlès, B., Marticorena, B., Mougin, E., Peugeot, C., Diedhiou, A., Haywood, J. M., Ngamini, J. B., Polcher, J., Redelsperger, J.-L., and Thorncroft, C. D.: The AMMA field campaigns: multiscale and multidisciplinary observations in the
15 West African region, *Q. J. Roy. Meteorol. Soc.*, 136, 8–33, 2009.
- Lee, T. J. and Pielke, R. A.: Estimating the soil surface specific humidity, *J. Appl. Meteorol.*, 31, 480–484, 1992.
- Lelay, M. and Galle, S.: How changing rainfall regimes may affect the water balance: a modelling approach in West Africa, *IAHS-AISH P.*, 2, 203–210, 2005.
- 20 Lohou, F., Saïd, F., Lohon, M., Durand, P., and Serça, D.: Impact of boundary-layer processes on near-surface turbulence within the West African Monsoon, *Bound.-Lay. Meteorol.*, 136, 1–23, 2010.
- Lohou, F., Kergoat, L., Guichard, F., Boone, A., Cappelaere, B., Cohard, J.-M., Demarty, J., Galle, S., Grippa, M., Peugeot, C., Ramier, D., Taylor, C. M., and Timouk, F.: Surface response to rain events throughout the West African monsoon, *Atmos. Chem. Phys. Discuss.*,
25 13, 18581–18620, doi:10.5194/acpd-13-18581-2013, 2013.
- Lothon, M., Saïd, F., Lohou, F., and Campistron, B.: Observation of the diurnal cycle in the low troposphere of West Africa, *Mon. Weather Rev.*, 136, 3477–3500, 2008.
- Mauder, M. and Foken, T.: *Documentation and Instruction Manual of the Eddy Covariance Software Package TK2*, Univ., Abt. Mikrometeorologie Bayreuth, 2004.
- 30 Mauder, M., Jegede, O. O., Okogbue, E. C., Wimmer, F., and Foken, T.: Surface energy balance measurements at a tropical site in West Africa during the transition from dry to wet season, *Theor. Appl. Climatol.*, 89, 171–183, 2007.

Daily and seasonal dynamics

O. Mamadou et al.

[Title Page](#)

[Abstract](#)

[Introduction](#)

[Conclusions](#)

[References](#)

[Tables](#)

[Figures](#)

[◀](#)

[▶](#)

[◀](#)

[▶](#)

[Back](#)

[Close](#)

[Full Screen / Esc](#)

[Printer-friendly Version](#)

[Interactive Discussion](#)



- Moore, C. J.: Frequency response corrections for eddy correlation systems, *Bound.-Lay. Meteorol.*, 37, 17–35, 1986.
- Parker, D. J., Burton, R. R., Diongue–Niang, A., Ellis, R. J., Felton, M., Taylor, C. M., Thorncroft, C. D., Bessemoulin, P., and Tompkins, A. M.: The diurnal cycle of the West African monsoon circulation, *Q. J. Roy. Meteorol. Soc.*, 131, 2839–2860, 2005.
- Philippon, N. and Fontaine, B.: The relationship between the Sahelian and previous 2nd Guinean rainy seasons: a monsoon regulation by soil wetness?, *Ann. Geophys.*, 20, 575–582, doi:10.5194/angeo-20-575-2002, 2002.
- Pospichal, B., Karam, D., Crewell, S., Flamant, C., Hünerbein, A., Bock, O., and Saïd, F.: Diurnal cycle of the intertropical discontinuity over West Africa analysed by remote sensing and mesoscale modelling, *Q. J. Roy. Meteorol. Soc.*, 136, 92–106, 2010.
- Ramier, D., Boulain, N., Cappelaere, B., Timouk, F., Rabanit, M., Lloyd, C. R., Boubkraoui, S., Métayer, F., Descroix, L., and Wawrzyniak, V.: Towards an understanding of coupled physical and biological processes in the cultivated Sahel – 1. Energy and water, *J. Hydrol.*, 375, 204–216, 2009.
- Sakaguchi, K. and Zeng, X.: Effects of soil wetness, plant litter, and under-canopy atmospheric stability on ground evaporation in the Community Land Model (CLM3.5), *J. Geophys. Res.*, 114, D01107, doi:10.1029/2008JD010834, 2009.
- Santanello, J. A. and Friedl, M. A.: Diurnal covariation in soil heat flux and net radiation, *J. Appl. Meteorol.*, 42, 851–862, 2003.
- Schmid, H. P.: Footprint modeling for vegetation atmosphere exchange studies: a review and perspective, *Agr. Forest Meteorol.*, 113, 159–183, 2002.
- Schotanus, P., Nieuwstadt, F. T. M., and De Bruin, H. A. R.: Temperature measurement with a sonic anemometer and its application to heat and moisture fluxes, *Bound.-Lay. Meteorol.*, 26, 81–93, 1983.
- Schüttemeyer, D., Moene, A. F., Holtslag, A. A. M., Bruin, H. A. R., and van Giesen, N: Surface fluxes and characteristics of drying semi-arid terrain in West Africa, *Bound.-Lay. Meteorol.*, 118, 583–612, 2006.
- Seghieri, J., Vescovo, A., Padel, K., Soubie, R., Arjounin, M., Boulain, N., de Rosnay, P., Galle, S., Gosset, M., Mouctar, A. H., Peugeot, C., and Timouk, F.: Relationships between climate, soil moisture and phenology of the woody cover in two sites located along the West African latitudinal gradient, *J. Hydrol.*, 375, 78–89, 2009.

- Séguis, L., Kamagaté, B., Favreau, G., Descloitres, M., Seidel, J.-L., Galle, S., Peugeot, C., Gosset, M., Le Barbé, L., Malinur, F., Van Exter, S., Arjounin, M., Boubkraoui, S., and Wubda, M.: Origins of streamflow in a crystalline basement catchment in a sub-humid Sudanian zone: the Donga Basin (Benin, West Africa): inter-annual variability of water budget, *J. Hydrol.*, 402, 1–13, 2011.
- Sellers, P. J., Heiser, M. D., and Hall, F. G.: Relations between surface conductance and spectral vegetation indices at intermediate (100 m² to 15 km²) length scales, *J. Geophys. Res.*, 97, 19033–19059, 1992.
- Sultan, B. and Janicot, S.: The West African monsoon dynamics, Part II: The “preonset” and “onset” of the summer monsoon, *J. Climate*, 16, 3407–3427, 2003.
- Taylor, C. M. and Lebel, T.: Observational evidence of persistent convective-scale rainfall patterns, *Mon. Weather Rev.*, 126, 1597–1607, 1998.
- Taylor, C. M., de Jeu, R. A. M., Guichard, F., Harris, P. P., and Dorigo, W. A.: Afternoon rain more likely over drier soils, *Nature*, 489, 423–426, 2012.
- Thornton, E.: Technical Description of version 4.0 of the Community Land Model (CLM), available at: <http://nldr.library.ucar.edu/repository/assets/technotes/asset-000-000-000-847.pdf> (last access: 29 May 2013), 2010.
- Timouk, F., Kergoat, L., Mougin, E., Lloyd, C. R., Ceschia, E., Cohard, J. M., Rosnay, P., Hiernaux, P., Demarez, V., and Taylor, C. M.: Response of surface energy balance to water regime and vegetation development in a Sahelian landscape, *J. Hydrol.*, 375, 178–189, 2009.
- United Nations, Department of Economic and Social Affairs, Population Division, World Population Prospects: The 2010 Revision, Press Release (3 May 2011): World Population to reach 10 billion by 2100 if fertility in all countries converges to replacement Level, 2011, available at: http://esa.un.org/unpd/wpp/other-information/press_release_wpp2010.pdf, (last access: 19 June 2013), 2011.
- van de Griend, A. A. and Owe, M.: Bare soil surface resistance to evaporation by vapor diffusion under semiarid conditions, *Water Resour. Res.*, 30, 181–188, 1994.
- Webb, E. K., Pearman, G. I., and Leuning, R.: Correction of flux measurements for density effects due to heat and water vapour transfer, *Q. J. Roy. Meteorol. Soc.*, 106, 85–100, 1980.
- Weiss, M., Baret, F., Smith, G. J., Jonckheere, I., and Coppin, P.: Review of methods for in situ leaf area index (LAI) determination: Part II. Estimation of LAI, errors and sampling, *Agr. Forest Meteorol.*, 121, 37–53, 2004.

Daily and seasonal dynamics

O. Mamadou et al.

Title Page

Abstract

Introduction

Conclusions

References

Tables

Figures

◀

▶

◀

▶

Back

Close

Full Screen / Esc

Printer-friendly Version

Interactive Discussion



HESSD

10, 10605–10657, 2013

Daily and seasonal dynamics

O. Mamadou et al.

Title Page

Abstract

Introduction

Conclusions

References

Tables

Figures

◀

▶

◀

▶

Back

Close

Full Screen / Esc

Printer-friendly Version

Interactive Discussion



- Wilson, K., Goldstein, A., Falge, E., Aubinet, M., Baldocchi, D., Berbigier, P., Bernhofer, C., Ceulemans, R., Dolman, H., Field, C., Grelle, A., Ibrom, A., Law, B. E., Kowalski, A., Meyers, T., Moncrieff, J., Monson, R., Oechel, W., Tenhunen, J., Valentini, R., and Verma, S.: Energy balance closure at FLUXNET sites, *Agr. Forest Meteorol.*, 113, 223–243, 2002.
- 5 Xue, Y. and Shukla, J.: The influence of land surface properties on Sahel climate, Part I: Desertification, *J. Climate*, 6, 2232–2245, 1993.
- Zeng, N., Neelin, J. D., Lau, K.-M., and Tucker, C. J.: Enhancement of interdecadal climate variability in the Sahel by vegetation interaction, *Science*, 286, 1537–1540, 1999.

Daily and seasonal dynamics

O. Mamadou et al.

Table 1. Instrumentation of Nalohou site.

Parameter (unit)	Sensor	Height a.g.l.	Accuracy	Sampling rate	Averaging interval
Air temperature (°C)	Vaisala WXT510 capacitive ceramic	2 m	±3 %	10 s	30 min
Relative humidity (%)	Vaisala WXT510 capacitive thin film polymer	2 m	±3 % [0–90 %], ±5 % [90–100 %]	10 s	30 min
Wind speed (ms ⁻¹) and direction (°)	Vaisala WXT510 ultrasonic anemometer	2 m	±0.3 ms ⁻¹ ±3°	10 s	30 min
Shortwave radiation incoming and outgoing (Wm ⁻²)	Kipp and Zonen CNR1 pyranometer 0.305 < λ < 2.8 μm	2 m	±10 % for daily sums	10 s	30 min
Longwave radiation incoming and outgoing (Wm ⁻²)	Kipp and Zonen CNR1 pyrgeometer 5 < λ < 50 μm	2 m	±10 % for daily sums	10 s	30 min
Rainfall (mm)	Précis Mécanique ABS3030 tipping bucket rain gauge	1.2 m	0.5 mm	pulse	30 min
Soil temperature (°C)	Campbell Sci. T107 thermistor	-0.1 m -0.2 m -0.4 m	< ±0.2 °C	10 s	30 min
Volumetric soil moisture (cm ³ cm ⁻³)	Campbell Sci. CS616 water content reflectometer	-0.1 m -0.2 m	±2.5 %	10 s	30 min
Sensible heat flux (Wm ⁻²)	Campbell Sci. CSAT3 3-D sonic anemometer	4.95 m	< ±4.0 cm s ⁻¹ (u, v) < ±2.0 cm s ⁻¹ (w)	20 Hz	30 min
Latent heat flux (Wm ⁻²)	Eurosep LI-7500 open path gas analyzer	4.95 m	0.0047 ppt H ₂ O	20 Hz	30 min

Title Page

Abstract

Introduction

Conclusions

References

Tables

Figures

I ◀

▶ I

◀

▶

Back

Close

Full Screen / Esc

Printer-friendly Version

Interactive Discussion



Daily and seasonal dynamics

O. Mamadou et al.

Table 2. Meteorological and turbulent flux daily mean (Mean), minimum (Min) and maximum (Max) for the four studied periods (P1, P2, P3 and P4). sd is the standard deviation of the minimum and maximum values during each 15-day period.

Variables and units	P1			P2			P3			P4		
	Mean	DOY 18–DOY 32 Min \pm sd	Max \pm sd	Mean	DOY 57–DOY 71 Min \pm sd	Max \pm sd	Mean	DOY 189–DOY 203 Min \pm sd	Max \pm sd	Mean	DOY 298–DOY 312 Min \pm sd	Max \pm sd
Tair (°C)	22.6	16.2 (\pm 1.2)	29.9 (\pm 1.5)	28.9	21.0 (\pm 1.4)	36.4 (\pm 0.8)	23.7	19.06 (\pm 1.1)	27.6 (\pm 1.7)	24.6	16.8 (\pm 2.1)	34.05 (\pm 0.4)
qa (gm ⁻³)	3.3	2.9 (\pm 0.3)	3.6 (\pm 0.3)	9.02	5.2 (\pm 1.8)	14.9 (\pm 2.8)	17.14	15.6 (\pm 0.9)	18.5 (\pm 0.7)	11.8	8.7 (\pm 2.2)	16.1 (\pm 3.1)
WindS (ms ⁻¹)	2.4	0.6 (\pm 0.3)	4.9 (\pm 0.6)	1.3	0.12 (\pm 0.05)	2.8 (\pm 0.4)	1.4	0.2 (\pm 0.1)	2.9 (\pm 0.9)	0.7	0.13 (\pm 0.03)	1.9 (\pm 0.3)
VPD (kPa)	2.4	1.4 (\pm 0.13)	3.8 (\pm 0.3)	2.9	0.9 (\pm 0.3)	5.2 (\pm 0.4)	0.6	0.3 (\pm 0.1)	1.3 (\pm 0.4)	1.7	0.3 (\pm 0.1)	4.1 (\pm 0.3)
SWin (Wm ⁻²)	229	-5 (\pm 0.5)	814 (\pm 47)	239	-5 (\pm 0.8)	851 (\pm 73)	184	-2 (\pm 0.5)	790 (\pm 177)	236	-6 (\pm 1.3)	859 (\pm 44)
SWout (Wm ⁻²)	44	2 (\pm 0.3)	148 (\pm 9)	48	2 (\pm 0.4)	165 (\pm 7)	31	0.2 (\pm 0.8)	121 (\pm 24)	32	-1 (\pm 0.8)	101 (\pm 8)
SWnet (Wm ⁻²)	185	-8 (\pm 0.6)	666 (\pm 39)	191	-8 (\pm 0.8)	686 (\pm 68)	153	-4 (\pm 0.7)	669 (\pm 153)	204	-6 (\pm 0.8)	760 (\pm 41)
LWin (Wm ⁻²)	331	309 (\pm 13)	358 (\pm 17)	392	362 (\pm 12)	424 (\pm 14)	409	379 (\pm 7)	434 (\pm 6.2)	380	353 (\pm 19)	415 (\pm 17)
LWout (Wm ⁻²)	449	380 (\pm 10)	588 (\pm 13)	501	414 (\pm 9)	655 (\pm 9)	446	420 (\pm 6)	490 (\pm 15)	447	393 (\pm 12)	529 (\pm 7)
LWnet (Wm ⁻²)	-118	-235 (\pm 15)	-65 (\pm 7)	-109	-237 (\pm 21)	-45 (\pm 10)	-37	-72 (\pm 10)	-7 (\pm 5)	-67	-120 (\pm 16)	-29 (\pm 12)
albedo (-)	0.19			0.2			0.15			0.13		
Rn (Wm ⁻²)	67	-96 (\pm 7)	442 (\pm 29)	82	-85 (\pm 9)	446 (\pm 42)	116	-37 (\pm 13)	488 (\pm 149)	137	-63 (\pm 13)	625 (\pm 78)
G (Wm ⁻²)	0.3	-88 (\pm 6)	174 (\pm 11)	1	-93 (\pm 8)	189 (\pm 14)	0	-48 (\pm 15)	88 (\pm 35)	0	-48 (\pm 7)	97 (\pm 14)
H (Wm ⁻²)	72	-26 (\pm 10)	326 (\pm 40)	72	-13 (\pm 7.5)	291 (\pm 38)	24	-17 (\pm 4)	103 (\pm 38)	69	-13 (\pm 10)	288 (\pm 51)
LE (Wm ⁻²)	7	1 (\pm 1.2)	17 (\pm 4)	10	-8.5 (\pm 10)	41 (\pm 30)	115	9 (\pm 13)	259 (\pm 58)	54	-1 (\pm 10.6)	167 (\pm 83)
Res (Wm ⁻²)	18	0	77 (\pm 28)	11	0	37 (\pm 53)	34	5 (\pm 11)	96 (\pm 61)	42	0	123 (\pm 58)

Title Page

Abstract

Introduction

Conclusions

References

Tables

Figures

◀

▶

◀

▶

Back

Close

Full Screen / Esc

Printer-friendly Version

Interactive Discussion



Daily and seasonal
dynamics

O. Mamadou et al.

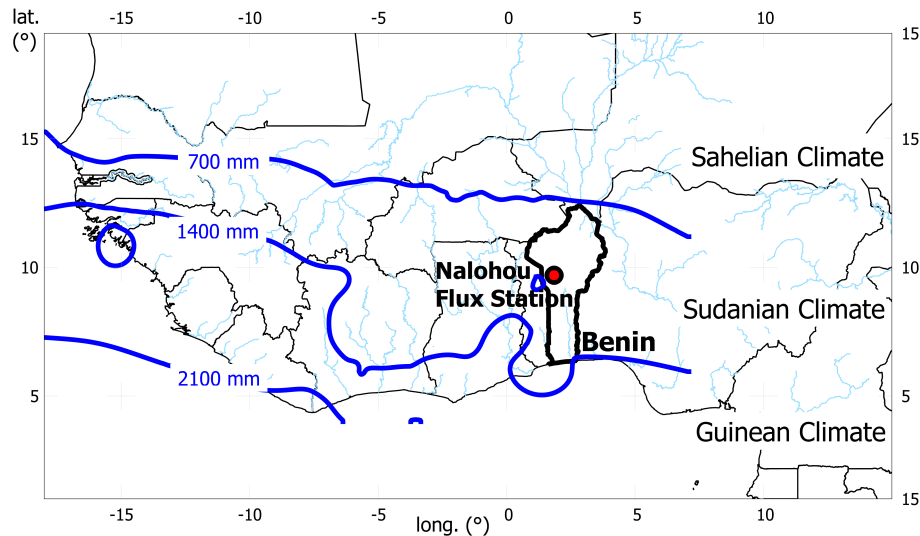


Fig. 1. Localization of the study area in West Africa. Blue lines are the 700, 1400 and 2100 mm isohyets computed from ground observations between 1950 and 2010. They define the different West African Climate areas: Sahelian, Sudanian and Guinean climates.

[Title Page](#)[Abstract](#)[Introduction](#)[Conclusions](#)[References](#)[Tables](#)[Figures](#)[I <](#)[> I](#)[◀](#)[▶](#)[Back](#)[Close](#)[Full Screen / Esc](#)[Printer-friendly Version](#)[Interactive Discussion](#)

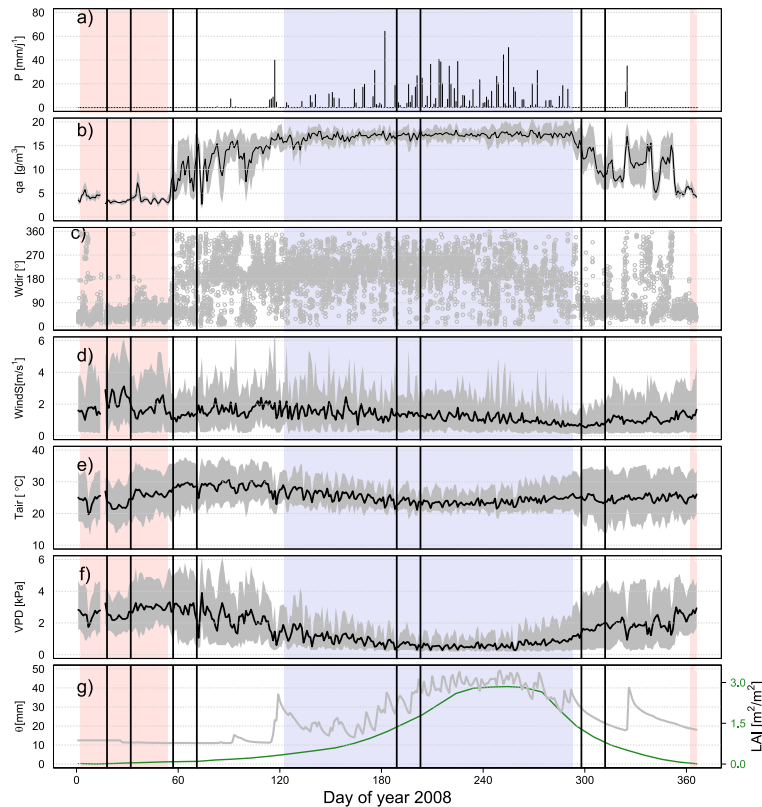


Fig. 2. Seasonal variation of meteorological variables. The black line is the daily average and the grey shaded areas the daily range of (a) precipitation, (b) absolute humidity, (c) 30 min wind direction, (d) wind speed, (e) air temperature, (f) vapor pressure deficit (VPD), (g) soil water content in the 0–30 cm layer (left axis) and leaf area index (LAI) (right axis). The rose and blue shaded areas underline respectively the dry and wet season according to q_a criterion. The vertical bars indicate the four studied periods.

[Title Page](#)
[Abstract](#)
[Introduction](#)
[Conclusions](#)
[References](#)
[Tables](#)
[Figures](#)
[◀](#)
[▶](#)
[◀](#)
[▶](#)
[Back](#)
[Close](#)
[Full Screen / Esc](#)
[Printer-friendly Version](#)
[Interactive Discussion](#)


Daily and seasonal dynamics

O. Mamadou et al.

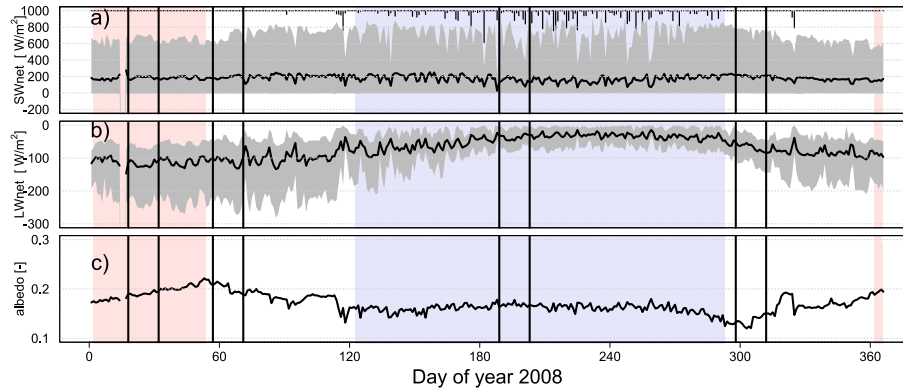


Fig. 3. Seasonal variation of radiation. The black line is the daily average and the grey shaded areas the daily range of **(a)** net shortwave radiation (SWnet), **(b)** net longwave radiation (LWnet) and **(c)** surface albedo. The rose and blue shaded areas underline respectively the dry and wet season according to q_a criterion. The vertical bars indicate the four studied periods.

[Title Page](#)[Abstract](#)[Introduction](#)[Conclusions](#)[References](#)[Tables](#)[Figures](#)[I◀](#)[▶I](#)[◀](#)[▶](#)[Back](#)[Close](#)[Full Screen / Esc](#)[Printer-friendly Version](#)[Interactive Discussion](#)

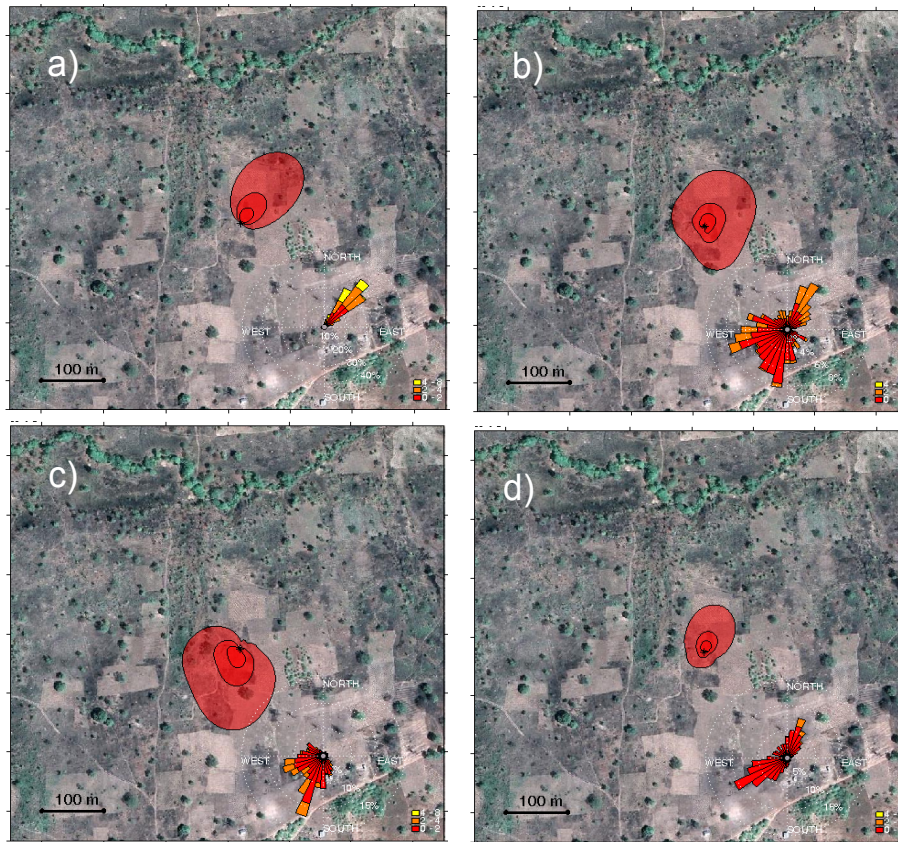


Fig. 4. Average footprint corresponding to each of the four selected periods superimposed over a Google Earth image (April 2010). Each iso-contour corresponds respectively to 25 %, 50 % and 75 % contribution to the sensible heat flux. The corresponding wind rose is shown in each plot for three wind speed classes: 0–2 m s^{-1} (red), 2–4 m s^{-1} (orange) and 4–6 m s^{-1} (yellow).

Daily and seasonal dynamics

O. Mamadou et al.

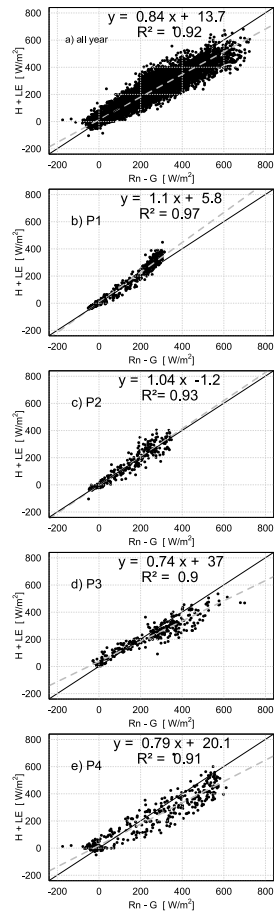


Fig. 5. Energy balance closure for the whole year **(a)** and the four studied periods: P1 **(b)**, P2 **(c)**, P3 **(d)** and P4 **(e)**.

[Title Page](#)[Abstract](#)[Introduction](#)[Conclusions](#)[References](#)[Tables](#)[Figures](#)[I ◀](#)[▶ I](#)[◀](#)[▶](#)[Back](#)[Close](#)[Full Screen / Esc](#)[Printer-friendly Version](#)[Interactive Discussion](#)

Daily and seasonal dynamics

O. Mamadou et al.

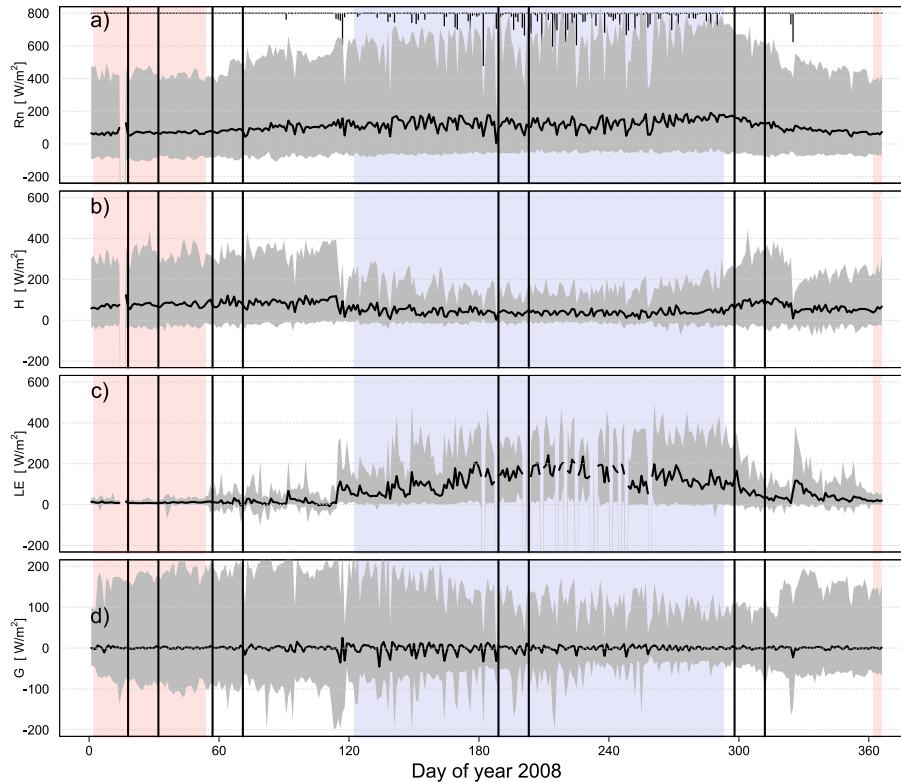


Fig. 6. Seasonal variation of energy fluxes. The black line is the daily average and the grey shaded areas the daily range of **(a)** net radiation (R_n), **(b)** sensible heat flux (H), **(c)** latent heat flux (LE) and **(d)** soil heat flux (G). The rose and blue shaded areas underline respectively the dry and wet season according to q_a criterion. The vertical bars indicate the four studied periods.

[Title Page](#)
[Abstract](#)
[Introduction](#)
[Conclusions](#)
[References](#)
[Tables](#)
[Figures](#)
[◀](#)
[▶](#)
[◀](#)
[▶](#)
[Back](#)
[Close](#)
[Full Screen / Esc](#)
[Printer-friendly Version](#)
[Interactive Discussion](#)

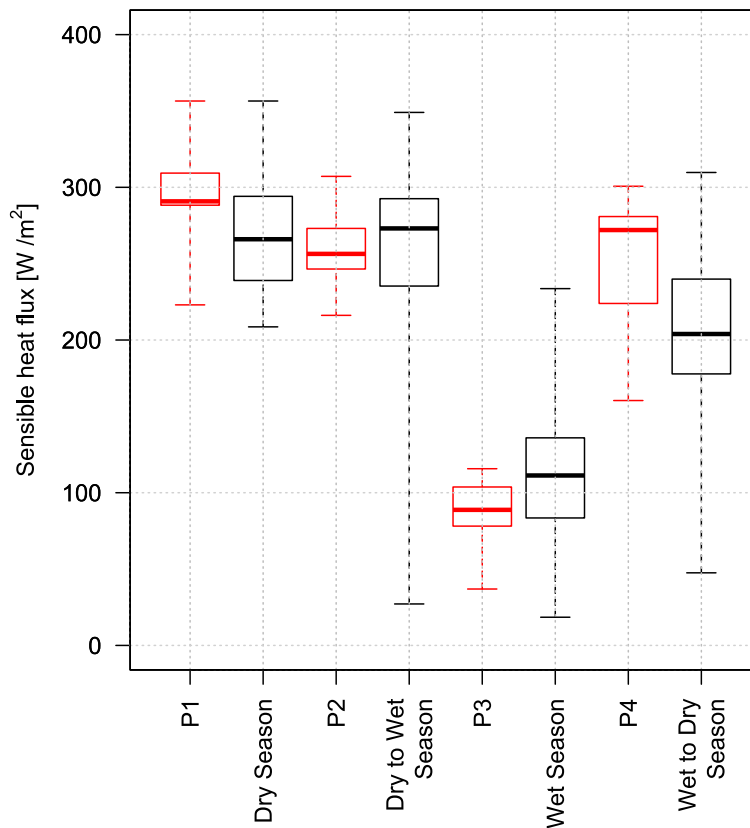



Fig. 7. Box plots of midday sensible heat flux (H) for the four studied periods (red) and the complete season (black). Each box represents the median, the 0.25 and the 0.75 quartiles; the whiskers indicate the maximum and the minimum values of H .

[Title Page](#)[Abstract](#)[Introduction](#)[Conclusions](#)[References](#)[Tables](#)[Figures](#)[◀](#)[▶](#)[◀](#)[▶](#)[Back](#)[Close](#)[Full Screen / Esc](#)[Printer-friendly Version](#)[Interactive Discussion](#)

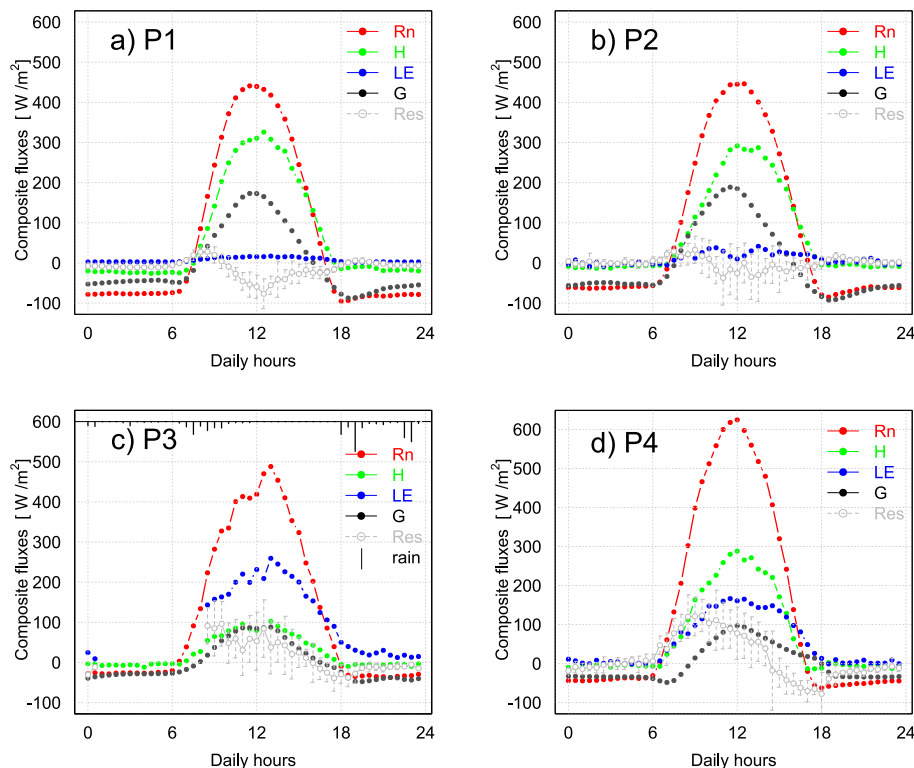


Fig. 8. Composite diurnal cycle of energy budget components for the four periods: **(a)** P1, **(b)** P2, **(c)** P3 and **(d)** P4. The net radiation (Rn), sensible heat flux (H), soil heat flux (G), latent heat flux (LE) and the residual of the energy balance equation ($\text{Res} = \text{Rn} - G - H - \text{LE}$) are plotted respectively in red, green, black, blue and grey. The grey brackets represent the residual standard deviation.

[Title Page](#)
[Abstract](#)
[Introduction](#)
[Conclusions](#)
[References](#)
[Tables](#)
[Figures](#)
[I ◀](#)
[▶ I](#)
[◀](#)
[▶](#)
[Back](#)
[Close](#)
[Full Screen / Esc](#)
[Printer-friendly Version](#)
[Interactive Discussion](#)


Daily and seasonal dynamics

O. Mamadou et al.

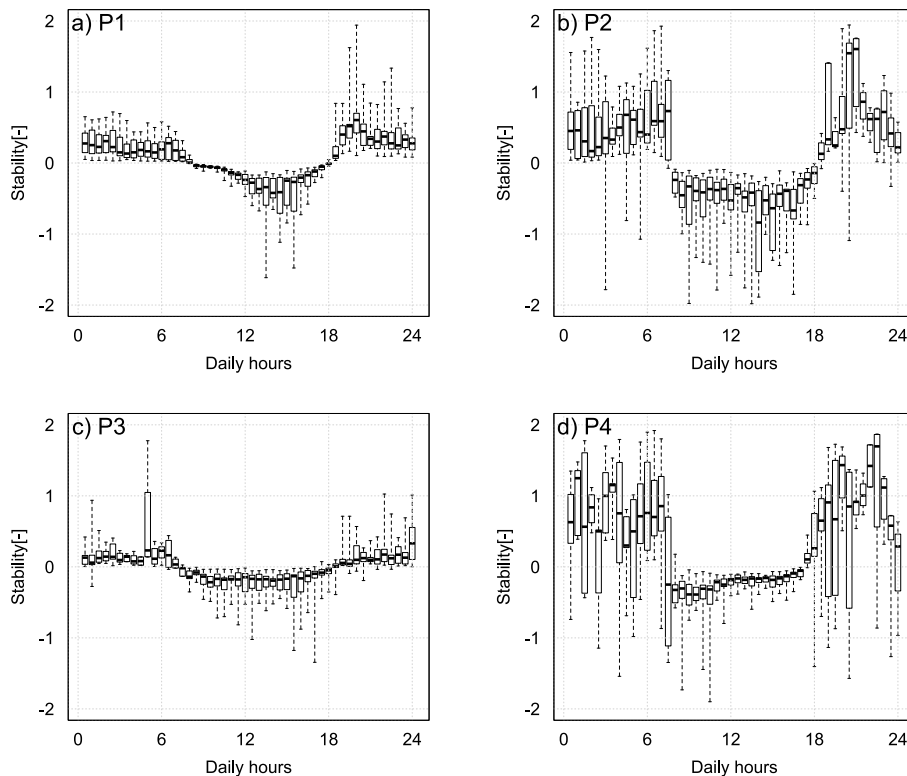


Fig. 9. Box plots of composite Monin–Obukhov stability at Nalohou site during (a) P1, (b) P2, (c) P3 and (d) P4. Each box represents the median, the 0.25 and the 0.75 quartiles; the whiskers indicate the maximum and the minimum values of the stability.

[Title Page](#)[Abstract](#)[Introduction](#)[Conclusions](#)[References](#)[Tables](#)[Figures](#)[◀](#)[▶](#)[◀](#)[▶](#)[Back](#)[Close](#)[Full Screen / Esc](#)[Printer-friendly Version](#)[Interactive Discussion](#)

Daily and seasonal dynamics

O. Mamadou et al.

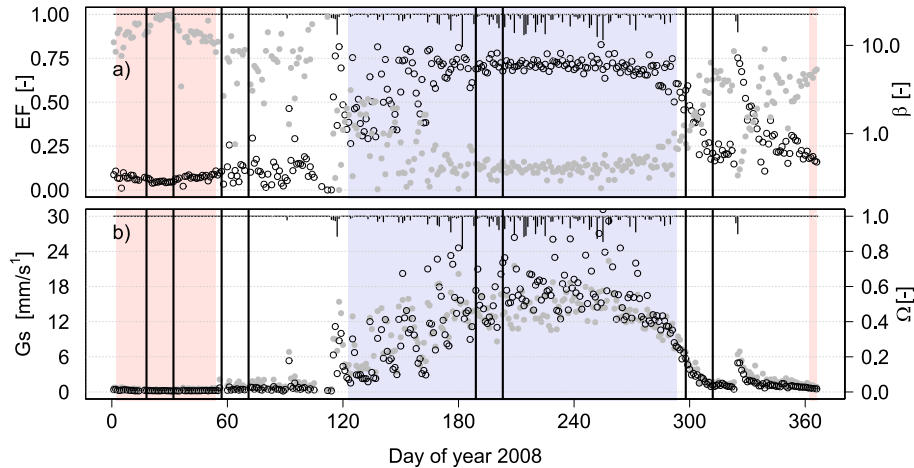


Fig. 10. Midday (10:00–14:00 UTC) average of **(a)** evaporative fraction (EF) (black circle – left axis), Bowen ratio (β) (grey points – right axis); **(b)** surface conductance (Gs) (black circle – left axis) and decoupling coefficient (Ω) (grey points – right axis). The rose and blue shaded areas underline respectively the dry and wet season according to q_a criterion. The vertical bars indicate the four studied periods.

[Title Page](#)
[Abstract](#)
[Introduction](#)
[Conclusions](#)
[References](#)
[Tables](#)
[Figures](#)
[◀](#)
[▶](#)
[◀](#)
[▶](#)
[Back](#)
[Close](#)
[Full Screen / Esc](#)
[Printer-friendly Version](#)
[Interactive Discussion](#)

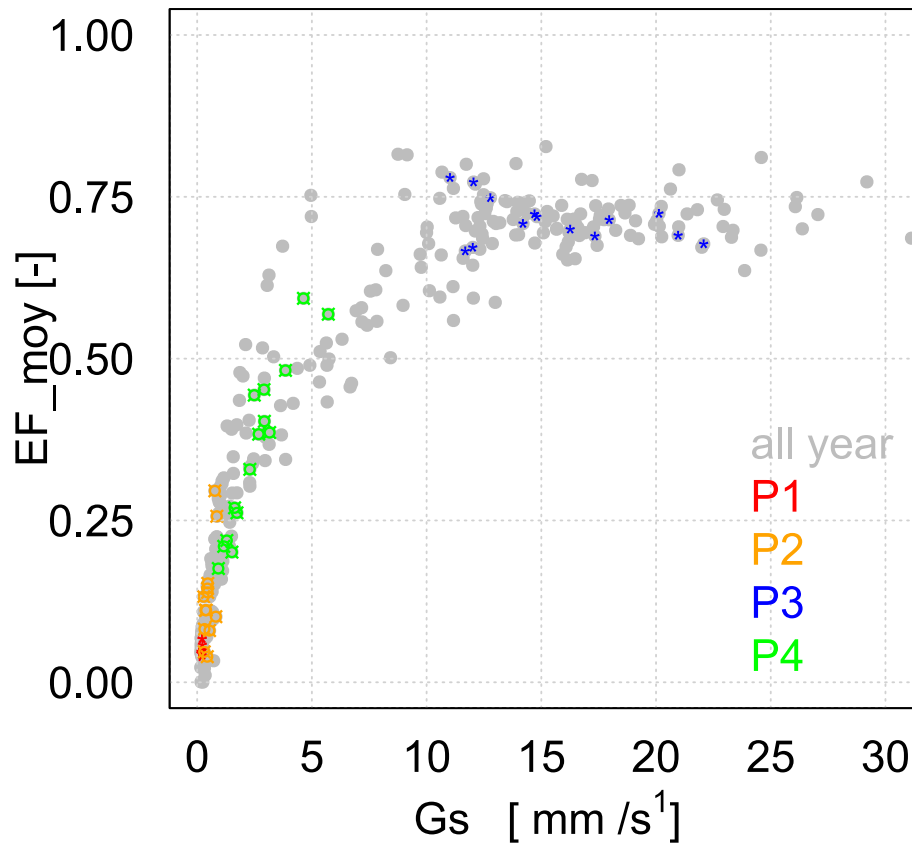



Fig. 11. Midday (10:00–14:00 UTC) evaporative fraction (EF_{moy}) vs. midday surface conductance (G_s) for the whole year (grey) and for the four periods: P1 (red), P2 (orange), P3 (blue) and P4 (green).

Title Page

Abstract

Introduction

Conclusions

References

Tables

Figures

◀

▶

◀

▶

Back

Close

Full Screen / Esc

Printer-friendly Version

Interactive Discussion



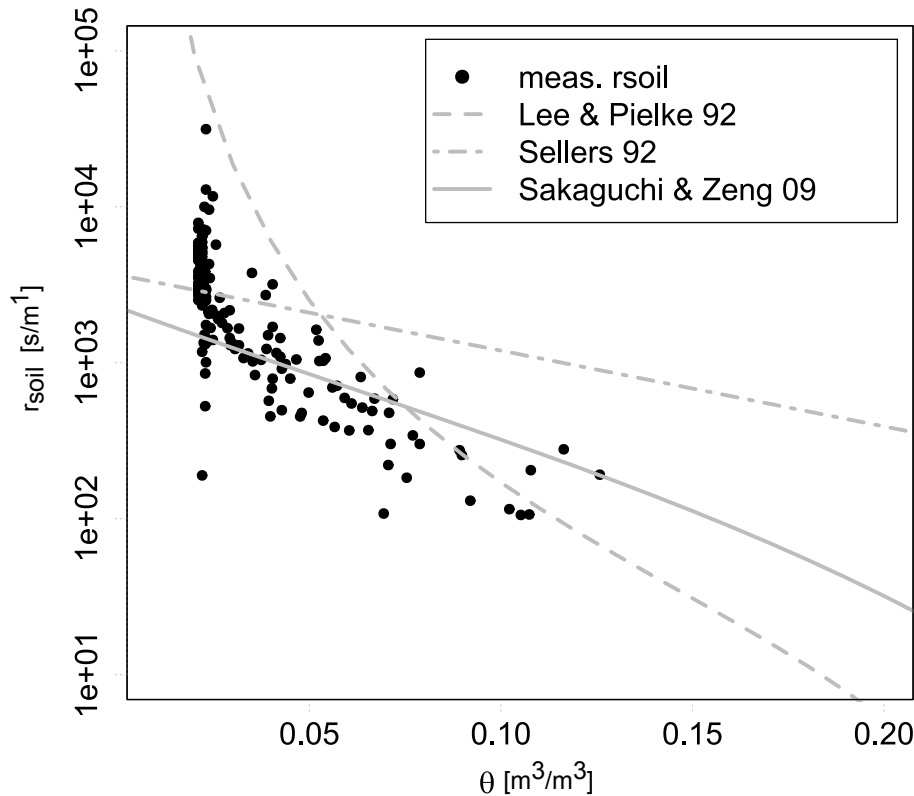


Fig. 12. Observed soil resistance (r_{soil}) against 5 cm soil moisture (θ) (black dot) and soil resistance model from Lee and Pielke (1992) (dashed line), Sellers (1992) (dash dotted line), and Sakaguchi and Zeng (2009) with curvature parameter $w = 5$ (thin line).

Title Page

Abstract	Introduction
Conclusions	References
Tables	Figures

⏪
⏩

◀
▶

Back	Close
------	-------

Full Screen / Esc

Printer-friendly Version

Interactive Discussion



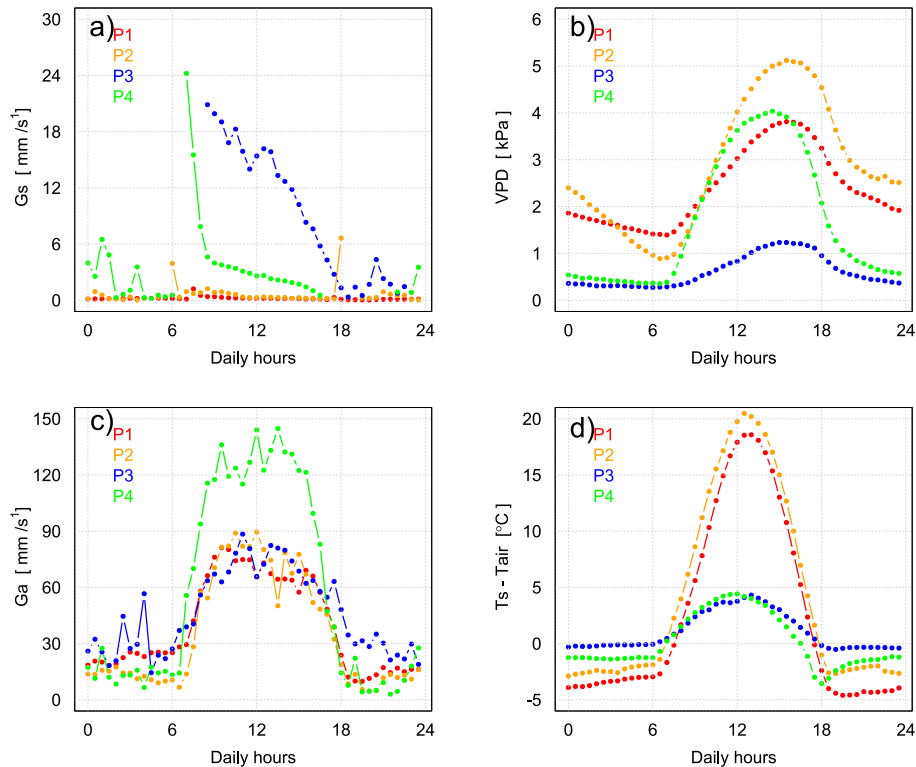


Fig. 13. Daily cycle of (a) surface conductance (G_s), (b) water vapor deficit (VPD), (c) aerodynamic conductance (G_a) and (d) temperature gradient between surface and air ($T_s - T_{\text{air}}$) for the four periods: P1 (red), P2 (orange), P3 (blue) and P4 (green).

Title Page

Abstract

Introduction

Conclusions

References

Tables

Figures

◀

▶

◀

▶

Back

Close

Full Screen / Esc

Printer-friendly Version

Interactive Discussion



Daily and seasonal dynamics

O. Mamadou et al.

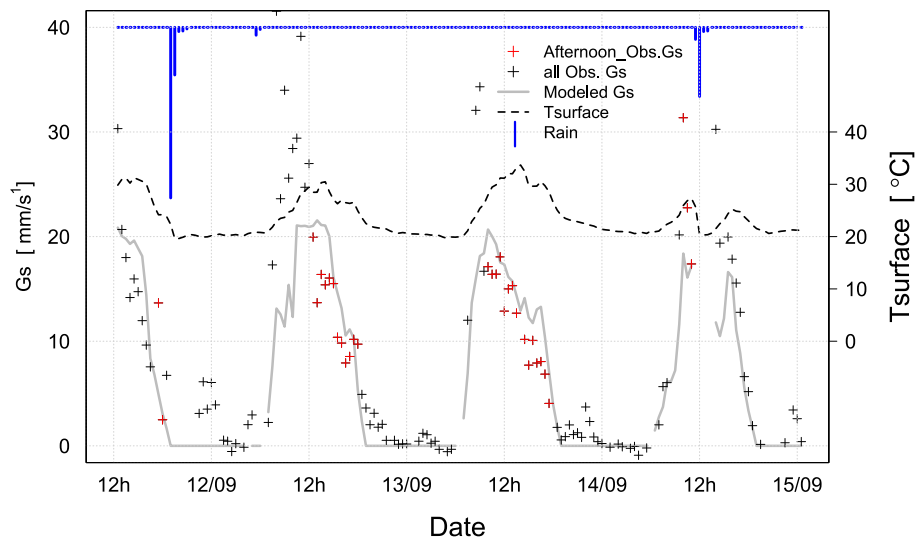


Fig. 14. Temporal variations of observed (cross) and modeled (grey line) surface conductance (G_s) for 3 typical wet season days (11 September to 15 September). The red crosses show the observations that are selected for further analysis. The blue vertical lines represent the rainy events, the dashed line the surface temperature (right axis).

[Title Page](#)
[Abstract](#)
[Introduction](#)
[Conclusions](#)
[References](#)
[Tables](#)
[Figures](#)
[◀](#)
[▶](#)
[◀](#)
[▶](#)
[Back](#)
[Close](#)
[Full Screen / Esc](#)
[Printer-friendly Version](#)
[Interactive Discussion](#)

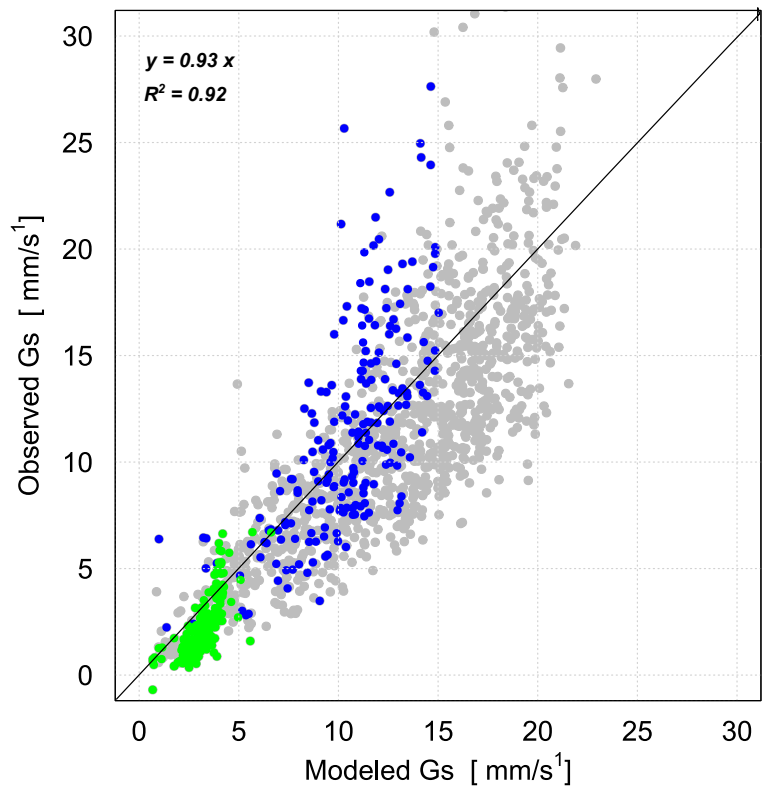



Fig. 15. Afternoon half-hourly observed against modeled (Ball–Berry) surface conductance (Gs) during the vegetated period (DOY 189–DOY 313) (grey dots). Superimposed blue (resp. green) dots stand for period P3 (resp. P4).

Title Page

Abstract

Introduction

Conclusions

References

Tables

Figures

⏪

⏩

◀

▶

Back

Close

Full Screen / Esc

Printer-friendly Version

Interactive Discussion



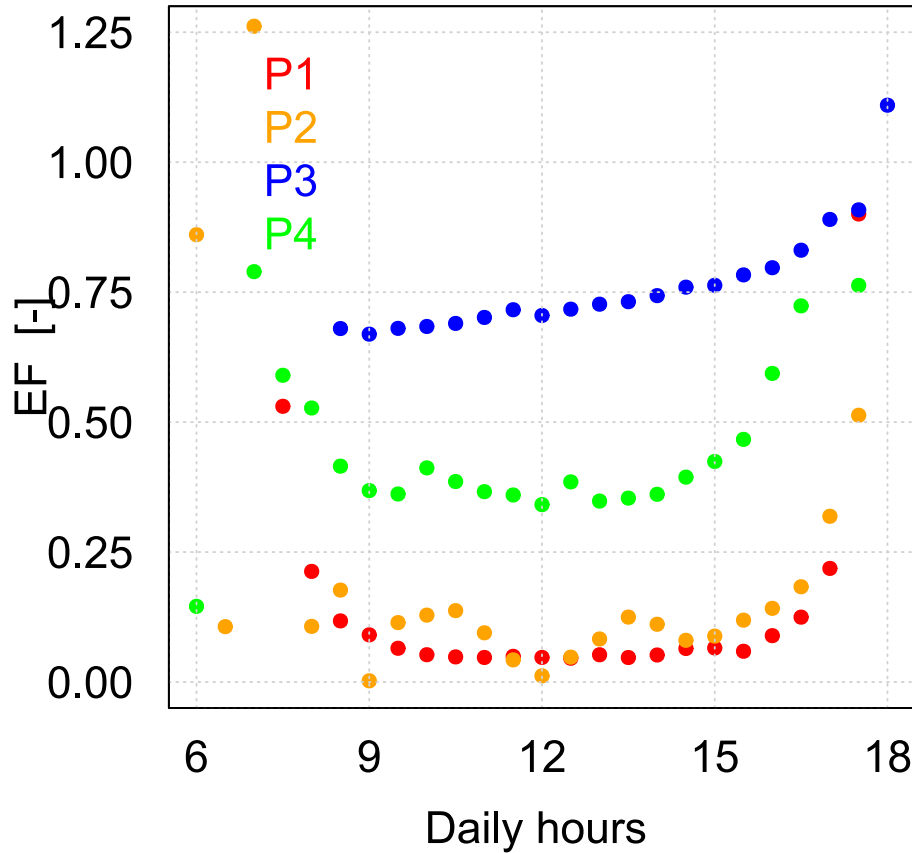


Fig. 16. Daily cycle of evaporative fraction (EF) for the four periods: P1 (red), P2 (orange), P3 (blue) and P4 (green).

HESSD

10, 10605–10657, 2013

Daily and seasonal dynamics

O. Mamadou et al.

[Title Page](#)

[Abstract](#) [Introduction](#)

[Conclusions](#) [References](#)

[Tables](#) [Figures](#)

[◀](#) [▶](#)

[◀](#) [▶](#)

[Back](#) [Close](#)

[Full Screen / Esc](#)

[Printer-friendly Version](#)

[Interactive Discussion](#)

